Aalto University
School of Electrical Engineering
Degree Programme in Automation and Systems Technology

Paula Sirén

Current density modelling in JET and JT-60U identity plasma experiments

Master's Thesis
Helsinki, May 7, 2013

Supervisor: Prof. Rainer Salomaa
Instructor: D.Sc. (Tech.) Tuomas Tala

Aalto University
School of Electrical Engineering
Degree Programme in Automation and Systems Technology

ABSTRACT OF
MASTER'S THESIS

Author: Paula Sirén

Title:
Current density modelling in JET and JT-60U identity plasma experiments

Date:	May 7, 2013	**Pages:**	60
Professorship:	Advanced Energy Technology	**Code:**	Tfy-56
Supervisor:	Prof. Rainer Salomaa		
Instructor:	D.Sc. (Tech.) Tuomas Tala		

The advanced tokamak scenarios have an important role in aiming to the steady-state operated fusion reactor. Time evolution of the safety factor q is connected to the total plasma current and confinement. In identity plasma experiments, two same-size tokamaks with similar plasma parameters are studied. Experiments in JET and JT-60U in 2008 were the first identity experiments on the largest operating tokamak devices in advanced scenarios. In this thesis, the previous data analysis has been extended with predictive current diffusion simulations by the 1.5-dimensional JETTO transport code.

The main objectives are to find the most significant reasons for the different time evolution of q and plasma current density components under the similarity conditions. Different properties (electron density and the shape of neutral beam current density profile) between the shots are characterised and the effect of the source terms (neutral beam driven current and internally generated bootstrap current) of current diffusion are also studied. In the theoretical part, current diffusion equation and the linear approximation of the generation of the bootstrap current are derived. The principles of the used codes for modelling of the transport effects, plasma equilibrium and NBI current are presented. Intensity of the effect of steeper density or temperature gradients and added external current components are quantified. In addition, the condition for the transition from the inductive H-mode to the steady-state operation is derived and the simulated cases are analysed.

Based on this analysis, the density gradient has the most important role in the different time evolution of the total plasma current density and q. Instead, the effect of the neutral beam current density is negligible. In JET, generating as large a bootstrap current fraction as in JT-60U requires a larger density gradient. A smaller fraction is not only caused by larger total plasma current but also by the weaker effect of the density gradient. In JET, retaining the steady-state q and current density profile requires a larger total pressure gradient than in JT-60U.

The critical bootstrap current density is studied for simulated cases but the experimental evidence of this transition-like effect has not been given. The quite rough approximation without the different gradients of electron and ion temperature and density does not possibly give the results which have been comparable with the experimental neoclassical bootstrap current. For this reason, some kind of a correction for the critical bootstrap current density is needed for the analysis with a higher accuracy. The reason for the different density peaking is not clarified by these current diffusion simulations. For this, predictive temperature and density simulations are required, which will be the first extended part of the forthcoming work.

Keywords: Fusion energy, Current density modelling, Bootstrap current, Advanced tokamak scenarios

Language: English

Aalto-yliopisto
Perustieteiden korkeakoulu

Aalto-yliopisto
Sähkötekniikan korkeakoulu
Automaatio- ja systeemitekniikan tutkinto-ohjelma

DIPLOMITYÖN TIIVISTELMÄ

Tekijä:	Paula Sirén		
Työn nimi:	Virrantiheysmallinnus JET- ja JT-60U-tokamakien identiteettiplasmakokeissa		
Päiväys:	7. toukokuuta 2013	**Sivumäärä:**	60
Professuuri:	Energiatieteet	**Koodi:**	Tfy-56
Valvoja:	Prof. Rainer Salomaa		
Ohjaaja:	TkT Tuomas Tala		

Jatkuvatoimisten skenaarioiden kehityksellä on keskeinen asema tähdättäessä kaupalliseen fuusioenergiaan. Varmuustekijän q aikakehitys on yhteydessä kokonaisplasmavirtaan ja plasman koossapitoon. Identiteettikokeissa tutkitaan kahden samankokoisen tokamak-laitteen toimintaa, kun plasmaparametrit on pyritty asettamaan mahdollisimman tarkasti toisiaan vastaaviksi. Ensimmäiset identiteettikokeet jatkuvatoimisissa skenaarioissa tehtiin vuonna 2008 maailman suurimmilla JET- ja JT-60U-tokamakeilla. Tässä työssä aiempaa data-analyysiä on laajennettu prediktiivisillä virtadiffuusiosimulaatioilla käyttäen 1,5-dimensioista JETTO-kuljetusyhtälökoodia.

Päätavoitteena työssä on löytää tärkeimmät syyt varmuustekijän ja plasmavirtakomponettien erilaiselle aikakehitykselle plasman ominaisuuksien ollessa mahdollisimman samankaltaisia. Plasmapulssien väliset erot (elektronitiheys ja neutraalihiukkasvirrantiheysprofiilin muoto) on selvitetty ja virtadiffuusion lähdetermien (neutraalihiukkasvirrantiheys ja sisäsyntyinen bootstrap-virrantiheys) vaikutusta tutkittu. Teoriaosuudessa on esitetty plasmavirrandiffuusioyhtälö ja johdettu neoklassisen sisäsyntyisen virran syntyä kuvaava lineaarinen approksimaatio. Kulkeutumisilmiöiden, plasman tasapainon ja neutraalihiukkasvirran mallintamiseen käytettyjen koodien pääperiaatteet on selostettu. Voimakkaan tiheysgradientin ja ulkoisten virrantiheyskomponenttien kuten mahdollisen alahybridiaaltovirran vaikutuksia on testattu. Tämän lisäksi on johdettu matemaattinen transitioehto induktiivisesta H-moodista jatkuvatoimiseen tilaan ja ehdon toteutumista on analysoitu simuloiduissa tapauksissa.

Analyysin perusteella tiheysgradientilla on merkittävin rooli plasmavirran ja q:n erilaisessa aikakehityksessä, mutta sen sijaan neutraalihiukkasvirrantiheyden merkitys on vähäinen. JET:ssä yhtä suuren bootstrap-virtaosuuden tuottamiseen tarvitaan suurempi tiheysgradientti kuin JT-60U:ssa. Tällöin stationaarisen virrantiheysprofiilin ja q:n saavuttaminen vaatii suuremman painegradientin. Kriittistä bootstrap-virrantiheyttä on analysoitu simuloiduissa tapauksissa, mutta transition kaltaisen ilmiön olemassaoloa ei ole kokeellisesti todistettu. Karkea approksimaatio ilman erillisiä lämpötila- ja tiheysgradientteja ei mahdollisesti anna vertailukelpoisia tuloksia kokeellisesti havaitun neoklassisen bootstrap-virran kanssa. Tästä syystä kriittisen bootstrap-virrantiheyden tarkempi analyysi vaatii korjaustermin lisäämistä kriittisen bootstrap-virrantiheyden lausekkeeseen.

Syytä tiheysprofiilin erilaiselle muodolle ei ole selvitetty näissä virtadiffuusiosimulaatioissa. Tätä voidaan tutkia laajentamalla analyysia prediktiivisillä lämpötila- ja tiheyssimulaatioilla.

Asiasanat:	Fuusioenergia, Virrantiheysmallinnus, Bootstrap-virta, Jatkuvatoimiset tokamak-skenaariot
Kieli:	Englanti

Preface

This work has been carried out at VTT Fusion and Plasma Technology group under the Euratom-Tekes Association. The project has been done mainly during the year 2012 as part of the ITER Scenario Modelling task force.

First and foremost, I would like to thank my instructor Dr Tuomas Tala at VTT and supervisor Prof. Rainer Salomaa at Aalto University for giving me the possibility to do this work and for the valuable help during the process — and for not losing their patience with my slightly non-physical approach on some phenomena.

Lots of thanks to Dr Xavier Litaudon at CEA for providing the topic, previous analysis and his help in the ITER Scenario Modelling group and also thanks to Dr Jeronimo Garcia at CEA for his interesting study which I could apply as a support for my analysis.

My gratitude goes also to Dr Antti Salmi at VTT for his useful help with ASCOT code and numerous computer problems as well as to Drs Gerard Corrigan and Florian Köchl at CCFE for their help with solving my problems with the JETTO code. Last but not least, Dr Jörg Hobirk at IPP Garching is acknowledged for kindly going through the thesis and for his extensive and needful comments.

Helsinki, May 7, 2013

Paula Sirén

Symbols

D	Deuterium
T	Tritium
He	Helium
R	Major radius coordinate
R_0	Reference major radius
r	Minor radius coordinate
a	Minor radius
ρ	Normalised toroidal coordinate
T_e, T_i	Electron or ion temperature
n_e, n_i	Electron or ion density
n_{tr}	Density of the trapped particles
τ_e	Energy confinement time
τ_{tr}	Banana orbit period
m_j	Mass of the particle j
e	Elementary charge
$v_j, v_{\perp,j}$	Velocity or perpendicular velocity of the particle j
$\vec{B}$	Magnetic field vector
B_ϕ	Toroidal magnetic field
B_θ	Poloidal magnetic field
B_0	Magnetic field at the reference major radius
Φ_{pr}, B_{pr}	Magnetic flux or field in the primary loop
M	Mutual inductance
I_{se}	Induced current in the secondary loop
I_p	Plasma current
A	Area
$\vec{J}$	Current density vector
j_ϕ	Toroidal current density
j_θ	Poloidal current density
j_{cd}	Current density component driven by external methods
j_{bs}	Component of the bootstrap current density
j_{nbi}	Current density component driven by neutral beams
$\vec{E}$	Electric field vector
E_ϕ	Toroidal electric field
p	Kinetic pressure
k_B	Boltzmann's constant
Z_j	Charge number of the particle j
Z_{eff}	Effective charge number

q	Safety factor
q_{95}	Safety factor at ρ=0.95
Q	Ratio of the output and input power
μ_0	Vacuum permeability
χ_{tot}	Total diffusion coefficient
χ_{neo}	Neoclassical diffusion coefficient
χ_{ano}	Anomalous diffusion coefficient
s	Magnetic shear
ν^*	Normalised collisionality
ν_{ei}	Electron-ion collisionality
ρ_L	Larmor radius
ρ^*	Normalised Larmor radius
ε	Inverse aspect ratio
ε_0	Vacuum permittivity
w	Banana width
u	Fluid velocity
$u_\parallel$	Parallel fluid velocity
ψ	Poloidal flux coordinate
F	Diamagnetic flux function
β	Ratio of the kinetic and magnetic energy
β_θ	Ratio of the kinetic and poloidal magnetic pressure
P_e	Power to electrons
P_i	Power to ions

Abbreviations

JET	Joint European Torus
JT-60U	Japanese Torus Updated
NBI	Neutral beam injection
RF	Radio frequency
BS	Bootstrap current
ITB	Internal transport barrier
MSE	Motional stark effect

Contents

1 Introduction

The response to increasing energy consumption requires development of new efficient methods for energy production. The field of several forms of energy production is very challenging: none of the present methods is able to take into account all unsolved problems such as limited resources of fuels or health, political and environmental aspects. Nuclear fusion is one of the most promising new solutions for a future energy source. Though it does not cause harmful pollution or long-term radioactive waste, and the fuel is inexpensive and easy to access, utilizing fusion reaction in energy production still requires better knowledge on plasma physical phenomena and more advanced technology.

Nuclear fusion is a reaction, where two light nuclei combine to form a heavier nucleus, and the internal energy of the system decreases. The difference of the internal energy is released as the kinetic energy of the product particles. The most important fusion reactions for the energy production are deuterium-deuterium (DD) and deuterium-tritium (DT) fusion which are described by the following reaction equations:

$$\mathrm{D} + \mathrm{D} \rightarrow {}^{3}\mathrm{He} + \mathrm{n} + 3.27\ \mathrm{MeV}$$

$$\mathrm{D} + \mathrm{D} \rightarrow \mathrm{T} + \mathrm{H} + 4.03\ \mathrm{MeV}$$

$$\mathrm{D} + \mathrm{T} \rightarrow {}^{4}\mathrm{He} + \mathrm{n} + 17.60\ \mathrm{MeV}.$$

In contrast to many other energy production methods, the fusion fuel is not expensive or difficult to purchase. There are 33 g of deuterium in a ton of sea water [1] from which it is easy to separate. Tritium for the DT fusion can be bred of lithium which is one of the most common metals in the Earth's crust. To the first wall of a DT fusion reactor, a lithium breeding blanket is intended to be installed; thus transporting of harmful radioactive tritium can be avoided. There are also safety limits set for the amount of tritium in a fusion reactor during its operation, due to the radiation safety of staff of the power plants.

The fusion reaction takes place by the quantum mechanical tunneling effect, when two nuclei penetrate the Coulomb potential barrier. The reaction needs high temperature of at least 10 keV, and the cross section of the reaction is very low. This is one of the most significant challenges of developing fusion for energy production. Sufficiently large temperature, density and confinement time are needed in commercial use of fusion energy. A simple criterion for the viable fusion reaction is defined by the fusion-triple product [2] with the relation

$$T_i n_i \tau_e \geq 10^{21} \mathrm{keV} \frac{\mathrm{s}}{\mathrm{m}^3}, \tag{1}$$

where n_i (m^{-3}) is the volume-averaged particle density, T_i (keV) is the ion temperature and τ_e is the confinement time of energy (s), where energy confinement is defined by the ratio of the internal energy of the system and the input power. In the current experimental devices, for instance the plasma shots which have been used with the modelling in this thesis, the achievable values for the density, temperature and confinement time are approximately 4–6$\times 10^{19}$ m^{-3}, 8–10 keV and 100–150 ms, respectively. This corresponds to a triple product value of 6–8$\times 10^{19}$ $\mathrm{keV}\frac{\mathrm{s}}{\mathrm{m}^3}$.

Peaceful fusion research for energy production started after the first international conferences for peaceful nuclear energy in the 1950's. In the 1960's the tokamak concept turned out to be the most promising candidate to the workable fusion reactor.

The tokamak-type fusion device was developed by the Soviet scientists Tamm and Sakharov in the late 1950's. Its main components are the toroidally shaped plasma chamber and toroidal and poloidal coils for confining the plasma with strong magnetic fields. In addition to the tokamak system, the particle sources and radio frequency antennas for heating and fuelling, diagnostic and measuring equipments and the divertor for power exhaust and collecting the impurities and the helium ash are needed. The schematic illustration of the most important parts of the tokamak is presented in Figure 1.

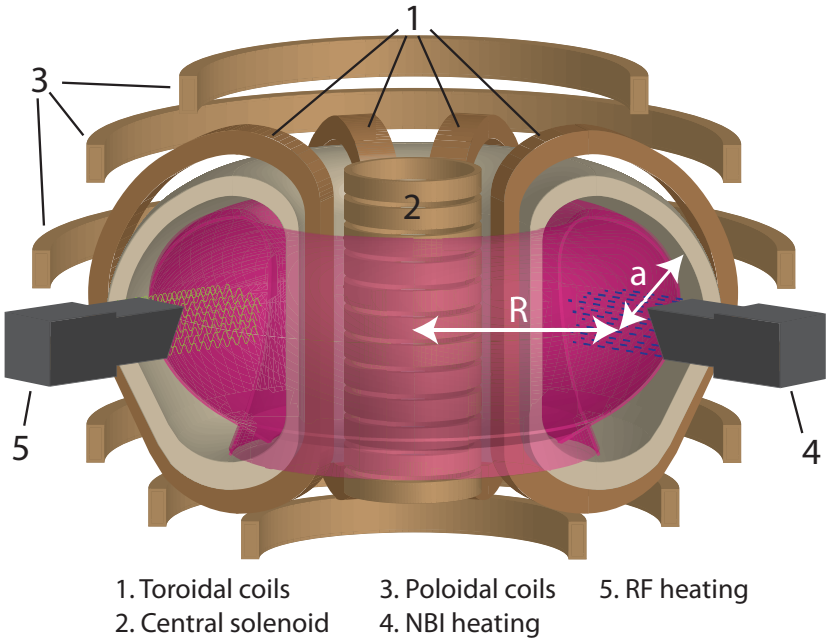

Figure 1: Main components of a tokamak.

The purpose of the toroidally shaped plasma chamber is to eliminate power and particle losses at the ends of a tubular chamber. The power losses are a significant challenge in developing fusion power plants for energy production. Losses are caused by conduction and convection over the separatrix and radiating impurities in the core plasma, most of which are released in plasma-wall interactions.

The structure of the wall of the plasma chamber of a future fusion reactor consists of the first wall, breeding blanket and radiation cover as shown in Figure 2. The first wall protects outer structures from particle and heat loads and also operates as a neutron multiplier for tritium breeding in the breeding blanket. The outermost layer of the wall structure is a radiation cover which mitigates the activation of the wall materials due to energetic neutrons, in particular in deuterium-tritium fusion.

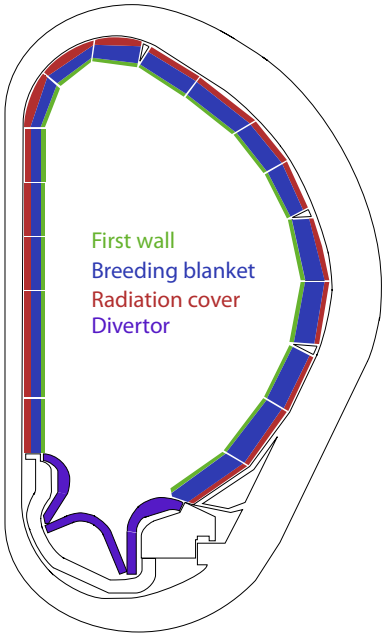

Figure 2: The structure of the wall of the plasma chamber of a future tokamak with the tritium breeding facilities.

The next massive step towards commercial fusion energy power plants is design and building of the largest tokamak-type experimental fusion device ITER in Cadarache in France. The main purpose of ITER is to prove the technical possibilities of nuclear fusion for commercial energy production. The goal of the ratio between the output and input power, or the Q value, is 10 with pulsed operation and 5 in steady state. The scale of dimensions compared to current tokamaks is huge: for instance the major radius is 6.2 m, volume 830 m^3 and the total current 9–15 MA in ITER [3]. For comparison, the corresponding values in the largest operating tokamak JET are 2.96 m, 80 m^3 and 0.7–4.5 MA [4].

In order to achieve a sufficiently high temperature and a sufficiently large non-inductive plasma current, heating and current-drive devices are essential components in a tokamak. At present, heating and especially current drive are partly based on electromagnetic induction, i.e., ohmic methods in the pulse-operated tokamaks. The aim of the future more advanced experimental fusion devices and power plants requires efficient methods for plasma current drive, since generating plasma current with non-ohmic methods is necessary in the steady-state fusion operation. With the efficient fusion devices that means developed external current drive methods, such as neutral beam injection and RF waves, and especially utilizing the self-generated neoclassical bootstrap current. [5] In ITER steady-state scenario the purpose is to produce 9 MA total plasma current and at least 50% from this by the self-generated bootstrap current [3]. This issue denotes that approximately 4–5 MA has to be produced by the external non-inductive methods.

The focus of this thesis is to analyse and clarify the plasma properties of

identity discharges (with same plasma parameters) in two large tokamak devices JET in UK and JT-60U in Japan on the basis of identity plasma experiments in advanced tokamak scenarios [6, 7]. The goals and the fundamental data analysis have been described in publication [6], and this work is its continuation whose meaning is to find the reasons for different behaviour of various plasma parameters. This is used as a basis for predictive current diffusion simulations with the 1.5-dimensional transport code JETTO [8] using experimental data of temperature and density profiles from JET and JT-60U.

The codes and the parts of the JETTO current diffusion model, which have been used in the simulations, are described in Section 3 and the validation and testing in Section 5. The main points of the identity experiments have been presented in Section 4. Based on these experimental results and the data analysis (described in Sections 4.1 and 4.2), the main differences between two tokamaks have been quantified.

The simulations concentrate on sorting out the current density components, in particular the significance of density gradients in increasing the bootstrap fraction. In addition, replacing the self-generated current components and steady-state condition (theoretical background presented in Section 2.5) with the help of the critical bootstrap current density have been discussed.

2 Plasma confinement and current drive

2.1 Plasma current

In a tokamak, plasma is kept away from the vessel walls by strong magnetic fields. The equation of motion of a charged particle in the electromagnetic field is

$$m_j \frac{d\vec{v}}{dt} = q_{\mathrm{j}} \left(\vec{E} + \vec{v} \times \vec{B} \right), \tag{2}$$

where $\vec{E}$ and $\vec{B}$ are the electric and magnetic fields and v_j, m_j and q_j the velocity, mass and electric charge of the particle j, respectively. The total magnetic field in toroidal geometry

$$\vec{B}_{tot} = \vec{B}_\phi + \vec{B}_\theta \tag{3}$$

is a helical sum of toroidal (ϕ) and poloidal (θ) components. The solution of Equation (2), i.e. the orbit of the particle, is a helical line which is described in yellow in Figure 3, where the radius of the yellow helical orbit is the Larmor radius ρ_L. The toroidal magnetic field is produced by the toroidal field coils (see Figure 1), whereas the poloidal component is induced by the plasma current.

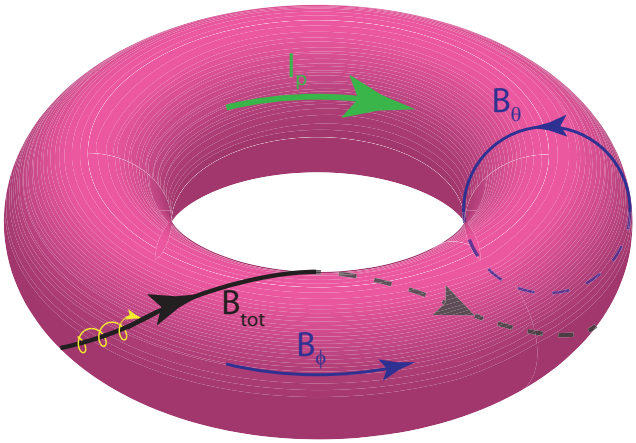

Figure 3: Components of the magnetic field in a tokamak and the helical orbit of a charged particle. Total toroidal plasma current I_p (produced by mutual induction in the central solenoid) is marked with green arrow.

The plasma current can be generated by ohmic and non-ohmic methods. The ohmic plasma current is generated by mutual induction, where the changing magnetic flux of the primary loop

$$\Phi_{pr} = \int \vec{B}_{pr} \cdot d\vec{A} \tag{4}$$

induces an electric current, I_{se}, in the plasma which operates as the secondary loop given by equation

$$\frac{d\Phi_{pr}}{dt} = M \frac{dI_{se}}{dt}, \tag{5}$$

where M is the mutual inductance of the loop system. The change of the primary magnetic flux is caused by the curl of the electric field defined by Faraday's equation

$$\nabla \times \vec{E}_{pr} = \frac{d\vec{B}_{pr}}{dt}, \tag{6}$$

where $\nabla \times \vec{E}_{pr}$ is caused by the changing current driven the central solenoid of a tokamak (see Figure 3). Non-ohmic plasma current can be generated by injecting neutral particles or emitting electromagnetic waves to the plasma, and non-ohmic methods are usable also for heating.

The total plasma current consists of the external and self-generated components

$$\vec{j}_{tot} = \vec{j}_{ohm} + \vec{j}_{cd} + \vec{j}_{bs}, \tag{7}$$

where $\vec{j}_{ohm}$ is the inductively generated current, $\vec{j}_{cd}$ is the current component produced by the external current drive methods and $\vec{j}_{bs}$ is the self-generated bootstrap current. Bootstrap current [9] has an important role in developing a steady-state fusion reactor. The self-generated current component increases the efficiency of the prospective nuclear fusion power plants, because, under certain conditions, it can cover over 50% of the total required plasma current [10]. Bootstrap current is caused by the pressure gradients in the plasma. By considering the form of the pressure gradient

$$\begin{aligned} \nabla p &= k_B n \nabla T + k_B T \nabla n \\ &= k_B \left(n_e \nabla T_e + \frac{1}{Z_{eff}} n_e \nabla T_i + \left(T_e + \frac{T_i}{Z_{eff}} \right) \nabla n_e \right), \end{aligned} \tag{8}$$

given by the ideal gas law, the connection between T_i, T_e and n_e can be noticed. Here Z_{eff} is the effective charge state and k_B is the Boltzmann's constant. More detailed discussion of the neoclassical bootstrap current is included in Section 2.4.

The externally driven current is produced mainly by neutral beam injection (NBI), or alternatively by radio frequency (RF) waves in recent tokamaks. The efficiency of these methods is based on energy transfer to plasma particles from injected fast neutral particles or electromagnetic waves. Challenges in external current-drive methods are not only sufficiently large current drive power: the shape of the produced current density profile influences the time evolution of the total plasma current profile and the confinement properties.

Neutral beam injection can be directed to the plasma parallel or perpendicular to the toroidal magnetic field which influences the direction of the plasma current. In current tokamaks, neutral beam injection is the most commonly used and well-known method for current drive, and it is further discussed in Section 3.2.

By utilizing the impact of the self-generated phenomena, the need for external current-drive methods can be decreased. However, it is significant for confinement to take into account the shape of the total current profile, so it is important to control the alignment of the bootstrap current density profile [6].

2.2 Safety factor and operational scenarios

The safety factor, q, is one of the most significant dimensionless plasma parameters for characterizing the confinement properties, and it is defined by the ratio

of the toroidal and poloidal magnetic field components in the plasma with the circular cross section by equation [11]

$$q = \frac{a}{R_0}\frac{B_\phi}{B_\theta} \approx \frac{2\pi r^2 B_\phi}{\mu_0 I(r) R_0}, \tag{9}$$

where a is the minor radius, R_0 the major radius and μ_0 is the permeability of the vacuum. The approximative form is the safety factor in the cylindrical geometry, where the connection between the safety factor and the total plasma current can be seen. By studying q, many important properties, for instance stability and steady state, can be clarified. Neoclassical diffusion coefficient, χ_{neo}, is related to q with connection

$$\chi_{neo} \sim \frac{q^4}{1+q^2} \sim q^2, \tag{10}$$

and it is related to the orbits of the particles with the Larmor radius

$$\rho_{L,j} = \frac{m_j v_\perp}{Z_j e B} \sim q^2, \tag{11}$$

which indicates that large values of q cause larger Larmor radius and degraded confinement. On the other hand, large q in the central plasma is connected to the forming of an internal transport barrier ITB (defined in Section 2.4) which causes the decreased anomalous transport and better confinement in the ITB region. Efficiency of fusion power is much better in these scenarios with smaller plasma current (in ITB region), if they can be sustained.

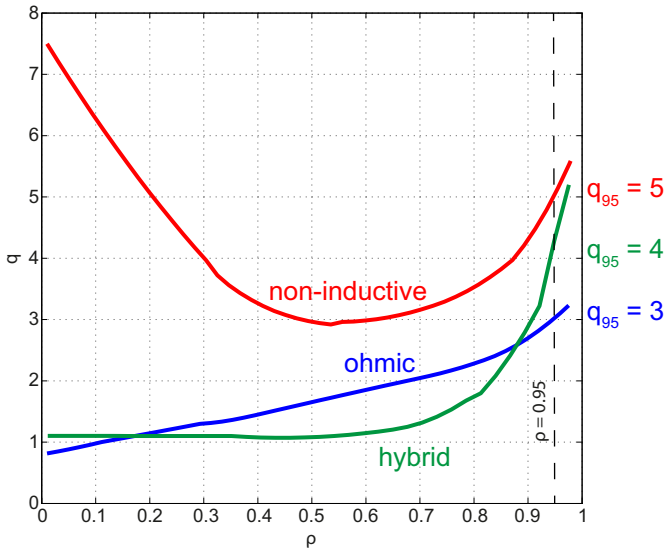

Figure 4: Operational scenarios classified by q-profile where the q_{95} is defined by the value of q when $\rho = 0.95$.

Different tokamak operational scenarios (pulse-operating baseline or ohmic scenario defined by $q_{95} = 3$ and advanced hybrid $q_{95} = 4$ or non-inductive $q_{95} \geq 5$ scenario) can be classified with the shape of the profile of the safety factor q and the magnetic shear s in Figure 4. Advanced tokamak scenarios can be defined by high fusion efficiency with operation close to steady state conditions and especially advanced scenarios with a reverse-shaped q-profile and a negative magnetic shear (defined by derivative of q with respect to the poloidal flux ψ) can be very important for studying the steady-state operation of forthcoming fusion reactors targeting to suppress the plasma turbulence and leading to enhanced confinement since, retaining the reverse shape of the q-profile is connected to triggering an ITB which decreases turbulence and makes confinement better [5].

2.3 Current diffusion

Diffusion of the magnetic field can be derived by starting from the Maxwell's equations for the curls of the electric and magnetic field $\vec{E}$ and $\vec{B}$:

$$\nabla \times \vec{E} = -\frac{\partial \vec{B}}{\partial t} \tag{12}$$

$$\nabla \times \vec{B} = \mu_0 \vec{J} \tag{13}$$

which give the connection between the electric and magnetic field and the current density $\vec{J}$.

The current density can be described with the help of the electric field in the field-theoretical form of the Ohm's law which causes the diffusing (ohmic) current component $\vec{j}_{ohm}$

$$\eta \vec{j}_{ohm} = \vec{E} + \vec{u} \times \vec{B}, \tag{14}$$

where η is the resistivity or magnetic diffusion coefficient and $\vec{u}$ the convection velocity of the fluid. Equation (14) can be inserted to equation (12), leading to the form

$$\nabla \times (\eta \vec{j}_{ohm} - \vec{u} \times \vec{B}_{tot}) = -\frac{\partial \vec{B}_{tot}}{\partial t}, \tag{15}$$

where $\eta \vec{j}_{ohm}$ describes diffusive and $\vec{u} \times \vec{B}_{tot}$ convective effects. Assuming that only the diffusion term is significant and the curl is taken from the both sides of equation, it gets the form

$$\frac{1}{\mu_0} \nabla \times \left(\nabla \times \left(\eta \vec{j}_{ohm} \right) \right) = -\nabla \times \left(\frac{d\vec{B}_{tot}}{dt} \right) = -\frac{\partial}{\partial t} \left(\nabla \times \vec{B}_{tot} \right), \tag{16}$$

where the order of the derivatives has been changed. The right side is

$$-\frac{\partial}{\partial t} \left(\nabla \times \vec{B}_{tot} \right) = -\mu_0 \frac{\partial \vec{j}_{tot}}{\partial t} \tag{17}$$

based on Equation (13). The left side can be rewritten by using vector-algebraic relations as

$$\frac{1}{\mu_0} \nabla \times \left(\nabla \times \left(\eta \vec{j}_{ohm} \right) \right) = \nabla \left(\nabla \cdot \left(\eta \vec{j}_{ohm} \right) \right) - \nabla^2 \left(\eta \vec{j}_{ohm} \right). \tag{18}$$

The first term is

$$\begin{aligned}
\nabla\left(\nabla\cdot\left(\eta\vec{j}_{ohm}\right)\right) &= \nabla\left(\nabla\eta\cdot\vec{j}_{ohm}+\eta\nabla\cdot\vec{j}_{ohm}\right)\\
&= \nabla\left(\nabla\eta\cdot\vec{j}_{ohm}+\frac{\eta}{\mu_0}\nabla\cdot\left(\nabla\times\vec{B}_{tot}\right)\right)\\
&= \nabla\left(\nabla\eta\cdot\vec{j}_{ohm}+\frac{\eta}{\mu_0}\left(\nabla\times\nabla\right)\cdot\vec{B}_{tot}\right)\\
&= 0, \qquad (19)
\end{aligned}$$

since $\nabla\eta \parallel \nabla T_e \parallel \vec{B} \perp \vec{j}_{ohm}$ and $\nabla\times\nabla = 0$. By using the total (which is the toroidal component in the tokamak case) plasma current density with Equation (7) the current diffusion equation with external source terms can be written in the form

$$\mu_0\nabla^2(\eta\vec{j}_{ohm}) = \mu_0\nabla^2(\eta(\vec{j}_{tot}-\vec{j}_{cd}-\vec{j}_{bs})) = -\mu_0\frac{d}{dt}(\vec{j}_{tot}). \qquad (20)$$

The equation is the universal form of the current diffusion equation which can be solved in the required geometry with a specific numerical method. Current diffusion in the plasma is predominantly a neoclassical phenomenon with the exception of some magnetohydrodynamical instabilities. Neoclassical theory gives an approach for the bootstrap current and resistivity.

2.4 Neoclassical transport

In this section, the background of the most important neoclassical effects in the tokamak is presented. The self-generated bootstrap current has a significant role in the current diffusion and achieving the steady-state operation. The objective of this section is to elucidate neoclassical transport theory, especially from the point of view of the bootstrap current and resistivity.

In a tokamak, neoclassical transport is the most dominant effect in many important fields. Classical transport describes the classical Coulomb collisions in a homogeneous magnetic field. Current diffusion in a tokamak is a neoclassical phenomenon, which means the classical effects with a correction due to the toroidal geometry. Neoclassical transport determines mainly internally generated bootstrap current and current diffusion coefficient or resistivity, but it plays a significant role also in ion heat conductivity and impacts anomalous-dominant transport effects caused by fluctuations of the electric and magnetic fields. [12, 13]

According to general diffusion theory, diffusion phenomena in plasma can be described with a coefficient χ,

$$\chi = \frac{(\Delta x)^2}{\Delta t} = \rho_L^2\nu, \qquad (21)$$

given by the collision frequency ν which corresponds to the relaxation time and a diffusion length equal to the Larmor radius ρ_L.

Neoclassical approach takes into account the effect of the magnetic mirror which induces the trapping of particles to the banana orbits (described in Figure 5). In the neoclassical theory, the width of the banana orbit defines the diffusion length (called banana width w) by equation [12]

$$\Delta x = \frac{\rho_L q}{\sqrt{\varepsilon}}, \tag{22}$$

so that, according to Equation (21)

$$\chi = \frac{\rho_L^2 q^2 \nu}{\varepsilon}, \tag{23}$$

where ε is the inverse aspect ratio

$$\varepsilon = \frac{r}{R}. \tag{24}$$

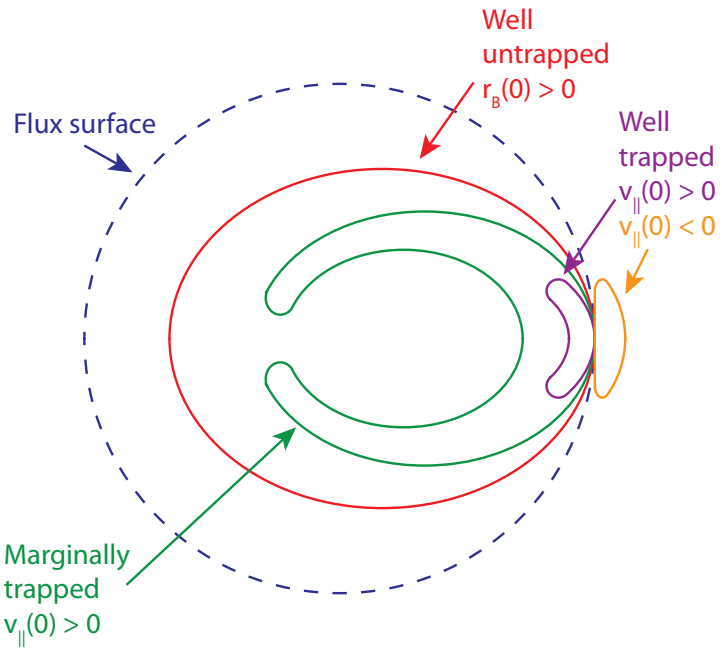

Figure 5: Banana orbits on the poloidal cross section.

The total diffusion coefficient consists of the the neoclassical and anomalous term

$$\chi = \chi_{neo} + \chi_{ano}. \tag{25}$$

The significance of the neoclassical component is the most dominant in current diffusion but it has to be taken into account in many anomalous-dominant diffusion processes like ion heat diffusion. In the anomalous transport phenomena, defining the diffusion coefficients is more complicated. Anomalous effects have to be taken into account when studying heat and particle transport with semi-empirical or complex theory-based transport models [12].

On the other hand, forming of an ITB leads to decreased anomalous transport (or turbulence modes), and here the fraction of neoclassical diffusion coefficient is larger with the exception of electron heat transport, where the neoclassical diffusion coefficient is negligible due to a small Larmor radius. An ITB

is defined by a locally decreased anomalous diffusion coefficient which is illustrated in Figure 6. Generally, the triggering of the ITB is connected to negative values of magnetic shear in the central plasma, which increases the neoclassical diffusion length. However, this effect may be much smaller than transport with non-suppressed turbulence modes.

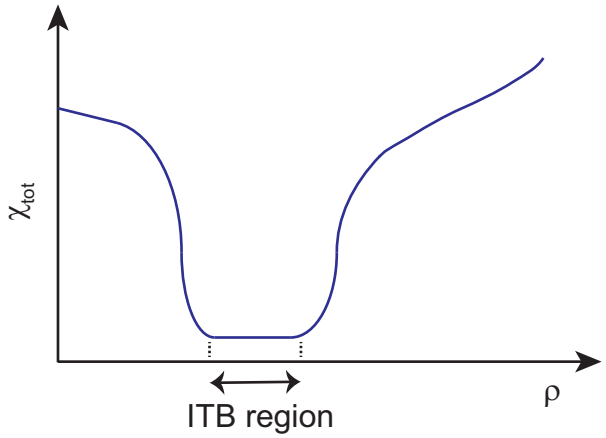

Figure 6: The definition of the internal transport barrier by the locally decreased diffusion coefficient.

The bootstrap current is generated by magnetic anisotropy, due to deviations from the magnetohydrodynamical stability which is presented in equation

$$\nabla p = \vec{j}_{tot} \times \vec{B}, \tag{26}$$

where the magnetic anisotropy induces a pressure gradient which is connected to balancing the plasma current density. Here, generating of the bootstrap current can be described in a simple way by a linear approximation inside the banana orbit (in the width of the banana, w, described in Figure 7, and w is assumed $\ll r$). The ratio of the trapped and passing particles is approximately determined by the connection [14]

$$n_{tr} = \sqrt{\varepsilon} n. \tag{27}$$

The trapped particles cause a current density, called the banana current, to the boundary of the banana orbit, given by [14]

$$j_b = Z_i e n^i_{tr} u_{\|}, \tag{28}$$

where n^i_{tr} is the density of the particle i and $u_{\|}$ the parallel fluid velocity. Here, the small change of density of the trapped particles and parallel velocity can be presented with equations

$$\delta n_{tr} = w\sqrt{\varepsilon}\frac{dn}{dr} \tag{29}$$

and

$$\delta u_{\|} = \sqrt{\varepsilon}\frac{du_{\|}}{dr} = w\sqrt{\varepsilon}\frac{du_{\|}}{dT}\frac{dT}{dr}. \tag{30}$$

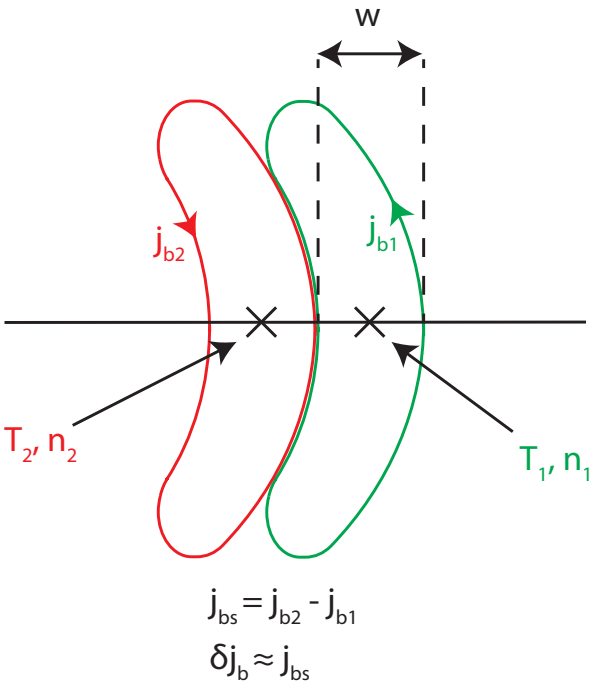

Figure 7: A schematic illustration of the forming of the bootstrap current at the edge of bananas.

The gradient of the trapped particle density or the parallel velocity cause a net current effect on the edge of the banana, which is illustrated in Figure 8. This current is called bootstrap current, and its mathematical relation can be derived starting from the moment balance equations [15]. The temperature gradient leads to larger bananas and a longer time τ_{tr} which particle needs to circle the whole banana orbit as shown in Figure 8b-c.

Now, a small change of banana current density or the linear approximation of the bootstrap current density is

$$\begin{aligned} \delta j_b &= e(\delta n_{tr} \cdot u_\parallel + \delta u_\parallel \cdot n_{tr}) \\ &= ew\sqrt{\varepsilon}\left(\frac{dn}{dr}u_\parallel + \frac{du_\parallel}{dT}\frac{dT}{dr}\right) \\ &= ew\varepsilon\left(\nabla n \cdot \sqrt{\frac{2T}{m}} + \frac{n}{\sqrt{2mT}}\nabla T\right), \end{aligned} \tag{31}$$

where $u_\parallel$ is defined by the average thermal velocity, v_{th}, according to

$$u_\parallel \approx \sqrt{\varepsilon} v_{th} = \sqrt{\frac{2T\varepsilon}{m}}. \tag{32}$$

The ratio of density- and temperature-driven components can be estimated with

the approximation

$$\frac{\delta j_b^{\nabla n}}{\delta j_b^{\nabla T}} \approx \frac{2T\nabla n}{n\nabla T}. \tag{33}$$

For the shot (JT-60U #49469, t = 7.0 s $\rho = 0.35$) which has been used this thesis, this approximation says that $j_{bs}^{\nabla n} \approx 5 j_{bs}^{\nabla T_e} \approx -10 j_{bs}^{\nabla T_i}$ in the ITB region.

A simple and applicable approximation with the pressure gradient can be presented by the following equation: [15]

$$j_{bs} = \varepsilon^{1/2} R \frac{\partial p}{\partial \psi}, \tag{34}$$

where ψ is the poloidal flux function. This form has been used when deriving the critical bootstrap current condition in the next section. More detailed form of the approximative bootstrap current, which takes into account the different effects of the pressure gradient, can be presented by equation [14]

$$\vec{j}_{bs} = -\sqrt{b}\frac{RB_\phi}{B_0}\left(2.44(T_e + T_i)\frac{dn}{d\psi} + 0.69n\frac{dT_e}{d\psi} - 0.42n\frac{dT_i}{d\psi}\right), \tag{35}$$

where $b = (B_{max} - B_{min})/(B_{max} + B_{min})$ describes the anisotropy of the magnetic field. The term $-\sqrt{b}B_\phi/B_0$ describes in more detail the same geometrical difference as the inverse aspect ratio in Equation 34.

Neoclassical resistivity, which describes the diffusion coefficient in current diffusion, is defined by equation [12]

$$\eta = \frac{m_e \langle \nu_{ei} \rangle}{n_e e^2}, \tag{36}$$

where m_e is the mass of an electron and $\langle \nu_{ei} \rangle$ is the collisionality of electrons and ions. Neoclassical resistivity is larger than classical form due to the trapped particles which do not contribute to the total toroidal plasma current.

Electron-ion collisionality describes the collision frequency of electrons with ions by Coulomb collisions and the approximative form can be written as

$$\nu_{ei} \approx \frac{\sqrt{2}}{64\pi}\frac{\omega_{pe}^4}{n_e}\left(k_B T_e\right)^{-3/2}, \tag{37}$$

where ω_{pe} is the plasma frequency

$$\omega_{pe} = \sqrt{\frac{n_e e^4}{\left(m_e \varepsilon_0\right)^2}}. \tag{38}$$

Where ε_0 is the permittivity of the vacuum. As stated in Equation (37), neoclassical resistivity is dependent on the electron temperature by $T_e^{-3/2}$, so the neoclassical current diffusion is reduced by the increased electron temperature.

The simple linear approximation, which was presented in this section, shows that the density gradient has a larger role in contributing to the bootstrap current than the temperature gradient. It means that forming of an internal transport barrier to the electron density is a very efficient way to increase the bootstrap fraction and to decrease the need for external current-drive methods.

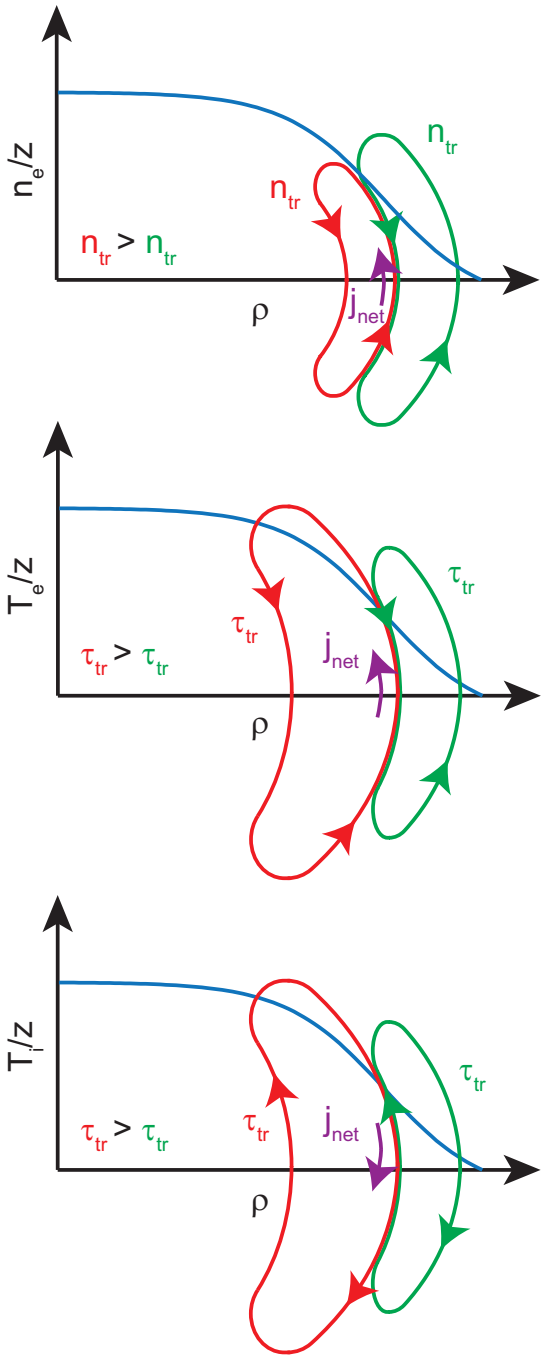

Figure 8: The effect of the net current on the edge of bananas with the density and temperature gradients.

2.5 Connection between poloidal current and high beta

A high poloidal beta ($\beta_p > 1$) is required for useful properties in fusion plasma: bootstrap fraction is proportional to the poloidal beta and the square root of the inverse aspect ratio [16]. Garcia et al. have presented an interesting method for checking conditions in a steady-state scenario with the poloidal current and critical bootstrap alignment [17] which is the basis of the formulae whose derivation and mathematical background is clarified in the following sections. Aiming at more efficient steady-state fusion reactor (with high beta), it is important to replace the ohmic current with other current components and to maximize the fraction of the self-generated component. [10, 15, 17]

By studying poloidal current density, the condition for the critical bootstrap current which is connected to high poloidal beta [17] can be derived. Steady-state properties of the plasma parameters can be assayed with the critical bootstrap current density condition which is derived in two following sections with the help of high beta and poloidal current density.

2.5.1 High beta values and poloidal current density

Beta denotes the ratio of the kinetic to the magnetic energy and it is defined by a volume-averaged pressure integral by equation [11]

$$\beta = \frac{2\mu_0}{B_0^2} \frac{\int p d\vec{S}}{\int d\vec{S}}, \tag{39}$$

where p is the kinetic pressure of the plasma and B_0 is the total magnetic field on the reference radius. Poloidal β takes into account only the magnetic pressure produced by poloidal magnetic field B_θ

$$\beta_\theta = \frac{2\mu_0}{B_{\theta \mathrm{a}}^2} \frac{\int p d\vec{S}}{\int d\vec{S}}. \tag{40}$$

Using cylindrical coordinates, the differential volume unit is defined by

$$\int d\vec{S} = \int_0^a 2\pi r dr = \pi a^2. \tag{41}$$

The pressure volume integral can thus be calculated by partial integral

$$\begin{aligned} \int p d\vec{S} &= \int_0^a 2\pi r p dr \\ &= \left|_0^a \big(2\pi r^2 p(r)\big) - 2\pi \int_0^a \frac{1}{2} r^2 \frac{dp}{dr} dr \right. \\ &= 2\pi a^2 p(a) - \pi \int_0^a r^2 \frac{dp}{dr} dr \\ &= -\pi \int_0^a r^2 \frac{dp}{dr} dr. \end{aligned} \tag{42}$$

Now it can be assumed that the pressure in the plasma boundary is zero, i.e., $p(a) \approx 0$, in which case

$$\beta_\theta = \frac{-2\mu_0 \int_0^a r^2 \frac{dp}{dr} dr}{B_{\theta a}^2 a^2}. \tag{43}$$

According to Ampere's law

$$\oint \vec{B} \cdot \vec{dl} = \mu_0 I_{enclosed}. \tag{44}$$

In a tokamak the magnetic field consists of a toroidal and a poloidal component. The toroidal component is perpendicular to the differential poloidal arc length element in equation (44). Thus

$$\begin{aligned} \oint \left(\vec{B}_\phi + \vec{B}_\theta\right) \cdot \vec{dl} &= \oint B_\theta dl \\ &= B_{\theta a} 2\pi a. \end{aligned} \tag{45}$$

Combining the results (44) and (45), the poloidal magnetic field in the plasma boundary is

$$B_{\theta a} = \frac{\mu_0 I_a}{2\pi a}, \tag{46}$$

where I_a is the total plasma current in the torus. Hence, according to Equation (40), β_θ can now be written as

$$\beta_\theta = -\frac{8\pi^2}{\mu_0 I_a^2} \int_0^a r^2 \frac{dp}{dr} dr. \tag{47}$$

In cylindrical coordinates the radial component of the magnetohydrodynamic equilibrium (Equation (26)) is

$$\frac{dp}{dr} = j_\theta B_\phi - \frac{B_\theta}{\mu_0 r} \frac{d(rB_\theta)}{dr}, \tag{48}$$

and poloidal beta becomes thus

$$\begin{aligned} \beta_\theta &= -\frac{2\mu_0}{B_{\theta a}^2 a^2} \int_0^a \left(j_\theta B_\phi - \frac{B_\theta}{\mu_0 r} \frac{d(rB_\theta)}{dr}\right) r^2 dr \\ &= -\frac{2\mu_0}{B_{\theta a}^2 a^2} \left(\int_0^a r^2 j_\theta B_\phi dr - \int_0^a r \frac{B_\theta}{\mu_0} \frac{d(rB_\theta)}{dr} dr\right). \end{aligned} \tag{49}$$

The second component of the sum is formed with

$$\int_0^a r \frac{B_\theta}{\mu_0} \frac{d(rB_\theta)}{dr} dr = \frac{1}{\mu_0} \int_0^a \left(B_\theta^2 r + B_\theta r^2 \frac{dB_\theta}{dr}\right) dr. \tag{50}$$

Partial integral gives this by expression

$$\begin{aligned} \frac{1}{\mu_0} \int_0^a \left(B_\theta^2 r + B_\theta r^2 \frac{dB_\theta}{dr}\right) dr &= \frac{1}{\mu_0} \left(\left|_0^a \frac{1}{2} B_\theta^2 r^2 - \int_0^a \frac{1}{2} B_\theta^2 \cdot 2r dr + \int_0^a B_\theta^2 r dr\right.\right) \\ &= \frac{1}{2\mu_0} \left|_0^a B_\theta^2 r^2 \right. \\ &= \frac{1}{2\mu_0} B_{\theta a}^2 a^2. \end{aligned} \tag{51}$$

Substituting this into Equation (49) gives

$$\begin{aligned}\beta_\theta &= -\frac{2\mu_0}{B_{\theta a}^2 a^2}\int_0^a r^2 j_\theta B_\phi dr + \frac{2\mu_0}{B_{\theta a}^2 a^2}\frac{1}{2\mu_0}B_\theta^2 a^2 \\ &= -\frac{2\mu_0}{B_{\theta a}^2 a^2}\int_0^a r^2 j_\theta B_\phi dr + 1. \end{aligned} \tag{52}$$

Equation (52) defines the border of the para- and diamagnetic plasma and it shows how beta is dependent on the poloidal current and high poloidal beta means that the poloidal current density is negative.

2.5.2 Critical bootstrap current density

In the previous section it has been presented, what kind of a dependence exists between the poloidal current density and the poloidal beta values. The connection between poloidal current density and bootstrap current density is known and it can be derived starting from the definitions of poloidal and toroidal current density in tokamak geometry.

Diamagnetic (or current) flux function F is defined by equation [11]

$$F = RB_\phi. \tag{53}$$

The derivative of the diamagnetic flux function with respect to the poloidal magnetic flux surface ψ is [17]

$$F' = \frac{\mu_0 R(j_\phi - Rp')}{F}. \tag{54}$$

The current components j_θ and j_ϕ are presented with a flux function F by

$$\begin{aligned} j_\theta &= F'\frac{B_\theta}{\mu_0} \\ &= \frac{\mu_0 R}{RB_\phi}(j_\phi - Rp')\frac{B_\theta}{\mu_0} \\ &= \frac{B_\theta}{B_\phi}(j_\phi - Rp') \end{aligned} \tag{55}$$

$$j_\phi = Rp' + \frac{FF'}{\mu_0 R} \tag{56}$$

which can be derived starting from the magnetohydrodynamical equilibrium and the definitions of flux functions. [11, 17]

Bootstrap current density depends on the inverse aspect ratio ε [15] by the general approximative form

$$j_{bs} \approx \varepsilon^{1/2} Rp'. \tag{57}$$

The following equation gives the connection between poloidal and bootstrap current densities

$$\begin{aligned} j_{bs} &= \left(\frac{B_\theta}{B_\phi}j_\phi - j_\theta\right)\frac{B_\phi}{B_\theta}\varepsilon^{1/2} \\ &= \varepsilon^{1/2}\left(j_\phi - j_\theta\frac{B_\phi}{B_\theta}\right). \end{aligned} \tag{58}$$

Now the bootstrap current fraction can be defined by

$$f_{bs} = \frac{j_{bs}}{j_\phi} = \varepsilon^{1/2}(1 - \frac{B_\theta}{B_\phi}), \tag{59}$$

when Equations (55) and (56) are used. Now, the so-called critical bootstrap current, corresponding to the case $F' = 0$, can be written as

$$\begin{aligned} j_{bs}^{crit} &= \frac{\varepsilon^{1/2}(j_{ohm} + j_{cd})}{1 - \varepsilon^{1/2}} \\ &= \frac{\varepsilon^{1/2}(\frac{E_\phi}{\eta} + j_{cd})}{1 - \varepsilon^{1/2}}, \end{aligned} \tag{60}$$

where E_ϕ is the toroidal electric field. This form is equal to zero poloidal current density profile [17]. If the condition of the critical bootstrap current density is radially mainly fulfilled, steady state in plasma can be achieved. This poloidal current alignment is the condition for the phase transition-like effect from a basic inductive H-mode [18] to a non-inductive advanced scenario [17], and it is a necessary condition for the (non-inductive) steady-state operation.

The need for the critical bootstrap current is very sensitive for small variations in the temperature and density profiles, which can be seen in time derivatives of Equation (60). This has to be noticed when calculating the critical bootstrap current alignment and explaining the results. By doing these two rough approximations (cylindrical geometry and $j_{bs} \sim \frac{\partial p}{\partial \psi}$) a simple analytical condition for critical bootstrap current density could be derived. In this thesis, the transition to the non-inductive state is studied with j_{bs}^{crit} due to more intuitive understanding than in the case of zero poloidal current density. Analysis of poloidal current density or defining diamagnetic current flux function requires a large accuracy from the equilibrium calculation method, so the approximate view can be noticed when interpreting these results. On the other hand, description of the critical bootstrap current density includes two significant approximations whose impact is difficult to estimate. For this reason, one has to be careful when drawing conclusions based on the critical bootstrap current condition. By using a different form of the bootstrap current density with better accuracy than the approximation with the pressure in Equation (57), the critical bootstrap current density is

$$j_{bs}^{crit} = \frac{(\varepsilon^{1/2} j_\phi + \xi)(\frac{E_\phi}{\eta} + j_{cd})}{(1 - \varepsilon^{1/2}) j_\phi - \xi}, \tag{61}$$

where the correction term is

$$\xi = j_{bs} - \varepsilon^{1/2} R p'. \tag{62}$$

By checking the correction term, the lower limit of the error of the critical bootstrap current can be estimated, if the ideal accuracy of the calculated j_{bs} is assumed.

3 Modelling tools

3.1 Plasma equilibrium

Toroidal symmetry is needed to make use of when considering transport effects with the two-dimensional approach on the poloidal flux surfaces ψ. In addition, by using the normalised toroidal coordinate

$$\rho = \sqrt{\frac{\phi}{\pi B_0}}, \tag{63}$$

transport effects can be described with one-dimensional partial differential equations if the quantities (for example pressure or q) are constant on the poloidal flux surface. Flux function ψ can be defined by solving the magnetohydrody-

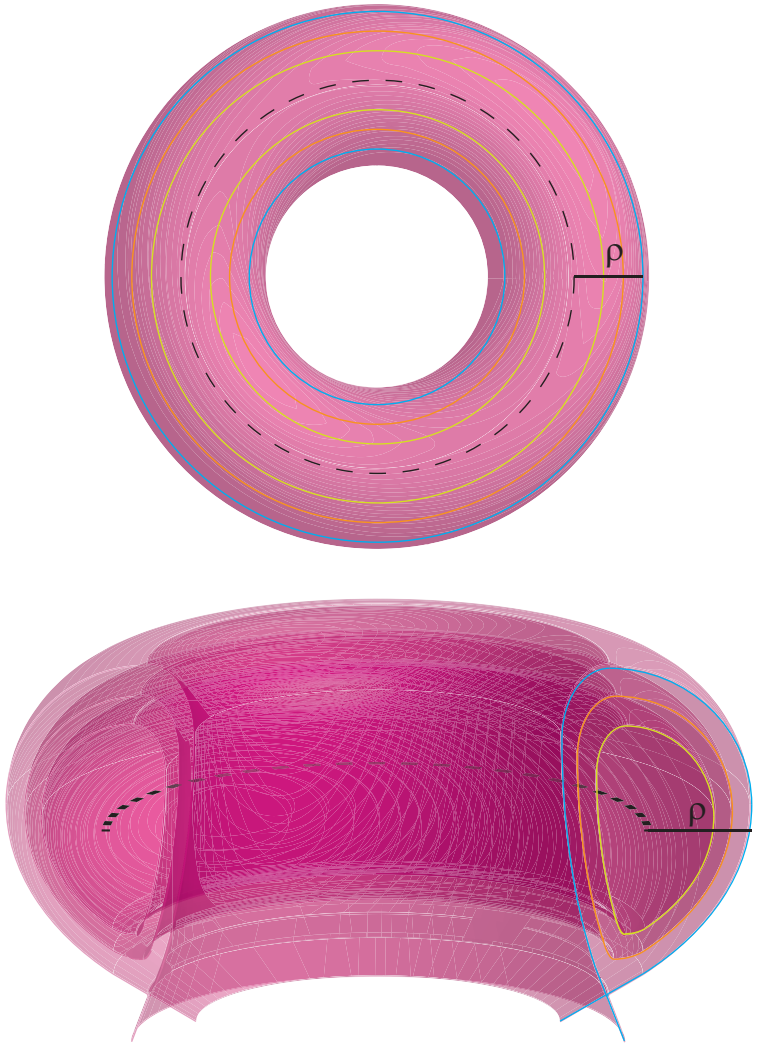

Figure 9: Simplifying 3-D torus geometry to 1-D toroidal ρ.

namical equilibrium (or the equilibrium of the kinetic and magnetic pressure) in the plasma (described in Equation (26)) on the flux surfaces which is described with the Grad-Shafranov equation which is a partial differential equation with respect to the poloidal magnetic flux function ψ and the current flux function F. By using the definitions of the toroidal current density (in Equation (56)) it can be derived with the curl of the poloidal magnetic field

$$\nabla \times \vec{B} = \nabla \times \left(\vec{B}_\phi + \vec{B}_\theta \right) = \mu_0 \left(\vec{j}_\theta + \vec{j}_\phi \right), \tag{64}$$

so that

$$\begin{aligned} \nabla \times \vec{B}_\theta &= \mu_0 \vec{j}_\phi \\ &= \left(\mu_0 R \frac{\partial p}{\partial \psi} + \frac{F}{R} \frac{\partial F}{\partial \psi} \right) \vec{e}_\phi. \end{aligned} \tag{65}$$

Due to the definition of the flux function ψ, the curl of the poloidal magnetic field can be presented with equation

$$\left| \nabla \times \vec{B}_\theta \right| = \frac{\partial}{\partial R} \frac{1}{R} \frac{\partial \psi}{\partial R} + \frac{1}{R} \frac{\partial^2 \psi}{\partial z^2}, \tag{66}$$

so Equation (65) gets a scalar form

$$\frac{\partial}{\partial R} \frac{1}{R} \frac{\partial \psi}{\partial R} + \frac{1}{R} \frac{\partial^2 \psi}{\partial z^2} = - \left(\mu_0 R \frac{\partial p}{\partial \psi} + \frac{F}{R} \frac{\partial F}{\partial \psi} \right) \tag{67}$$

which is called the Grad-Shafranov equation.

In the transition-like effect from an inductive H-mode to a non-inductive scenario (equal to the zero poloidal current density) [17], Grad-Shafranov equation is

$$\frac{\partial}{\partial R} \frac{1}{R} \frac{\partial \psi}{\partial R} + \frac{1}{R} \frac{\partial^2 \psi}{\partial z^2} = -\mu_0 R \frac{\partial p}{\partial \psi}. \tag{68}$$

The non-inductive state can be characterized with the values of the derivative of the flux function F. In ITB scenarios, the pressure gradient is negative, so a negative F' increases the absolute value of the toroidal current density in the ITB region. Instead, a positive F' decreases the magnitude of the toroidal current density, so it seems that same p' produces smaller current with positive F' (which is equal to positive poloidal current density as discussed in Sections 2.5.1 and 2.5.2).

In the simulations of this thesis, plasma equilibrium (flux functions ψ and F) is defined by ESCO or EFIT [19] code with MSE measurements. ESCO finds the numerical solution of the Grad-Shafranov equation (partial differential equation in spatial coordinates) with given plasma boundary and reference magnetic field. Instead, EFIT uses the magnetic measurement (for instance pressure, poloidal beta and internal inductance) by constraints in Picard iterations for defining ψ and F [19]. EFIT calculation can achieve a good accuracy which is dependent on magnetic measurement errors. For this reason, an EFIT equilibrium requires a correction in the central plasma where the measured data are not available. This is implemented by using in addition MSE (angle of poloidal and toroidal magnetic field) measurements in the central plasma region by constraints in the iteration. This method is the most accurate method for defining the equilibrium and the MSE measurements are required especially with reverse-q plasmas.

ESCO is the only available method for defining the plasma equilibrium in JT-60U for JETTO transport simulations. Before the current-diffusion simulations, the equilibriums given by different codes (ESCO, EFIT, EFIT-MSE) were compared. Differences between the EFIT-MSE and ESCO equilibrium were negligible but the location of the EFIT equilbrium (or centre of plasma) surfaces is moved with respect to the EFIT-MSE equilibrium. Analysing the poloidal current density (which needs the flux functions F) requires the same method the defining the equilibrium for all cases which is need to be compared. Also, current diffusion is not sensitive to small deviation of equilibrium, so ESCO could be selected for defining the plasma equilibrium in JETTO simulations.

3.2 JETTO transport code

JETTO is a 1.5-dimensional transport code for solving time-space partial differential equations in diffusion processes in the core plasma. It is connected to many different models with different approaches to the JETTO code for example for plasma equilibrium, neutral beam injections and diffusion coefficients. Modelling of transport phenomena in the plasma is based on solving the following four equations: [8]

$$\frac{3}{2}\left(\frac{dV}{d\rho}\right)^{-\frac{5}{3}}\frac{\partial}{\partial t}\left(\left(\frac{dV}{d\rho}\right)^{\frac{5}{3}}n_eT_e\right)+\left(\frac{dV}{d\rho}\right)\frac{\partial}{\partial\rho}\left(\frac{dV}{d\rho}\left\langle\nabla p\right\rangle^2\left(q_e+\frac{5}{2}T_e\Gamma_e\right)\right)=\langle P_e\rangle \quad (69)$$

$$\frac{3}{2}\left(\frac{dV}{d\rho}\right)^{-\frac{5}{3}}\frac{\partial}{\partial t}\left(\left(\frac{dV}{d\rho}\right)^{\frac{5}{3}}\sum_{j=1}^{n_H}n_jT_j\right)+\left(\frac{dV}{d\rho}\right)\frac{\partial}{\partial\rho}\left(\frac{dV}{d\rho}\left\langle\nabla p\right\rangle^2\left(\sum_{j=1}^{n_H}q_j+\frac{5}{2}T_i\Gamma_i\right)\right)=\langle P_i\rangle \quad (70)$$

$$\left(\frac{dV}{d\rho}\right)^{-1}\frac{\partial}{\partial t}\left(\left(\frac{dV}{d\rho}\right)^{-1}n\right)+\left(\frac{dV}{d\rho}\right)\frac{\partial}{\partial\rho}\left(\frac{dV}{d\rho}\left\langle\nabla p\right\rangle^2\Gamma\right)=\langle S_n\rangle \quad (71)$$

$$\frac{\partial\psi}{\partial t}=\frac{A\eta_{\|}}{\rho\mu_0}\frac{\partial}{\partial\rho}\left(K\frac{\partial\psi}{\partial\rho}\right)+\frac{V'\eta_{||}}{2\pi\rho}(j_{bs}+j_{cd}), \quad (72)$$

where V is the volume, ρ is the normalized toroidal flux coordinate, Γ is the particle or heat flux and S, P_e, P_i are the particle and heat sources. The current diffusion equation corresponds to Equation (20) in the toroidal geometry: ψ is the poloidal flux function and A and K are geometrical scaling factors. The space dependence of the equations is defined with the toroidal normalized flux coordinate ρ (defined by Equation (63))and q (or poloidal magnetic field) is described with the poloidal flux surface function ψ.

In this thesis, current diffusion equation is in the most attention by describing significant time-evolution effects in the plasma, so it is derived in Section 2.3 in the simple cylindrical geometry with the help of the Maxwell's equations. Generally, fluid approach-based transport equations can be derived starting from determinig the moments of kinetic equations. The kinetic or microscopic approach by the Fokker-Planck equation describes the time-spatial behaviour of the distribution function of the particle (electron or ion) number in the velocity space [13]

$$\frac{\partial f}{\partial t}+\vec{v_j}\cdot\frac{\partial f}{\partial\vec{r}}+\frac{Z_je}{m_j}(\vec{E}+\vec{v}\times\vec{B})\cdot\frac{\partial f}{\partial\vec{v}}=C+S, \quad (73)$$

where f is particle distribution function, C is a collisional factor and S is a source term.

The moments of the given function f with respect to $\vec{v}$ are defined by integrating over the total volume with a multiplication of $|\vec{v}|$ according to

$$M_n = \int |\vec{v}|^n f d\vec{V}. \tag{74}$$

This way, the ion or electron energy conservation equations can be derived by determining the second moments or particle transport equation by determining the zeroth moment of both sides of the Fokker-Planck equation. [13]

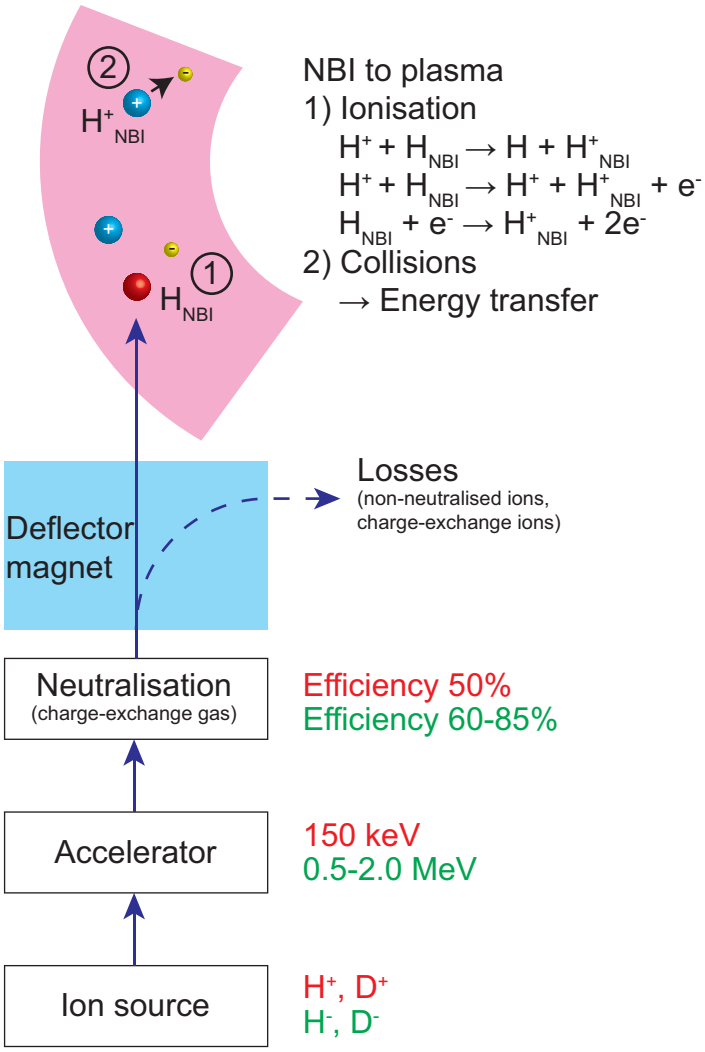

Figure 10: Components of the system for producing energetic neutral particles and their reactions in the plasma. Properties of the current devices are described in red and new ITER-relevant solutions in green.

3.3 Neutral beam injections

The NBI system for plasma heating and current drive consists of an ion source, a particle accelerator, a neutraliser and a deflector magnet, and the simple block diagram of the structure is presented in Figure 10. [20] In general, the whole NBI system of a tokamak includes several particle sources directed to the plasma with the different values of angles ϕ and θ. The absorbed power depositions and contribution to the total plasma current depend on the directions of the NBI sources which are presented in Figure 11. Normally-directed neutral beams give the heating power but the contribution to the toroidal plasma current is low. Instead, the tangential beams can produce a significant part of the non-inductive current. Angle θ defines the shape of the power deposition profile or the depth of the power absorption. By changing the angle θ, the on/off-axis current components can be controlled. Normally, the NBI system includes several NB sources directed with different angles. For example in JET the NBI system includes two NB boxes. One box has eight NB sources (with different but fixed angles ϕ and θ), half of which are tangential-like and half normal-like directed.

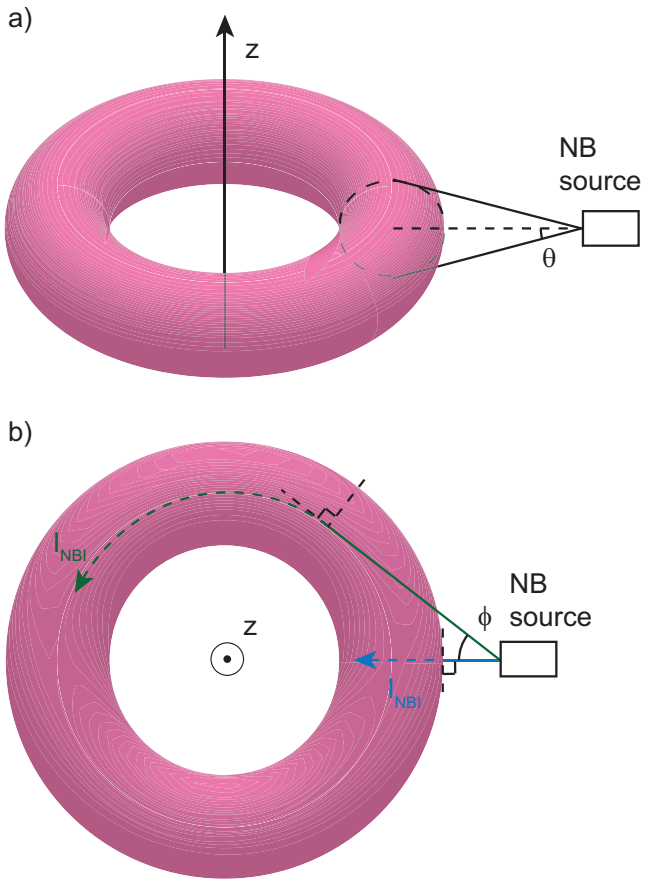

Figure 11: Direction of the neutral beam injections with help of toroidal- and poloidal-like angles ϕ and θ.

Positive-charged ions are easier to produce, and positive ion sources are used in current tokamaks. In ITER, negatively charged ion sources are required due to the need for higher-energy particles which are able to penetrate to the central plasma. Neutralisation is based on the charge-exchange reaction in the neutraliser gas. The cross section of the charge-exchange reaction (for positive ions) with high energies is quite small and the efficiency of the neutralisation is approximately 50% [20]. Instead, neutralisation of negative ions (even with energetic negative ions) is easier (efficiency 60-85% [20]), which is the reason why the negatively charged ions will be used in the future. [21]

Neutralised high-energy particles are directed to the plasma, and neutralisation losses (non-neutralised particles from the neutraliser gas) are separated with the deflector magnet. In the plasma, neutral particles can react with three different reactions: charge-exchange and ionization with electrons or ions [12]. The collisions between thermal plasma particles and fast injected particles lead to energy transfer (heating) and producing the external non-ohmic current.

In current diffusion modelling, the source term j_{nbi} is defined with the fluid (PENCIL) or kinetic (ASCOT) approach but these differences are not so significant by using the given profile by the source. The fluid code PENCIL determines the absorbed power-density profile from the ionisation profile (or ionisation probability). Instead, ASCOT takes the ionisation profile as an initial condition for solving the orbits of single fast NB particles. By considering this effect with the fluid view, the detailed information of the velocity distribution has been lost. The velocity distribution can be an important factor for instance when studying fast particles and power-deposition profiles. In the case of NB-current modelling, the kinetic approach means Monte Carlo simulation of a large amount of particles and solving the 7-dimensional Fokker-Planck equation in the target volume. On the other hand, kinetic single-particle following requires much more computing time, and in some cases differences between fluid approach are negligible. Hence, different NBI options have been tested before selecting the NBI-computing method for the current-diffusion simulations and the most important remarks are presented in Section 5.1.

The kinetic approach is very suitable to use when clarifying detailed behaviour in a small volume, but it is too slow method for studying the global phenomena over the whole torus, since it requires following of thousands of particles. In case the computation power is limited, by using a fluid-based code the differential equation system needs to be calculated only once in every time step, so it is a faster and the only (suitable) way to model effects in a large volume. [24]

4 Identity plasma experiments

Many properties of the plasma behaviour can be surveyed by considering the dimensionless plasma parameters. Similarity or identity of two or several plasma shots can be defined with the correspondence of dimensionless and dimensional plasma parameters. When studying two or more plasmas in different tokamaks, it is useful to compare the following most common dimensionless plasma parameters: normalized Larmor radius ρ_e^*, collisionality ν^*, ratio of the kinetic to magnetic energy β and safety factor q, which are defined by equations [25]

$$\rho_e^* = \frac{(m_e)^{1/2}}{e} \frac{(T_e)^{1/2}}{aB_0} \tag{75}$$

$$\nu^* = \left(\frac{R_0}{r}\right)^{3/2} qR\nu_{ei} \left(\frac{m_e}{2T_e}\right)^{1/2} \tag{76}$$

$$\beta = \frac{2p}{\mu_0 B_0^2} \tag{77}$$

$$q = \frac{r}{R_0} \frac{B_\phi}{B_\theta}. \tag{78}$$

Dimensionless parameters can be determined in a global or local form. Typically in experiments, plasma parameters are used in their global forms, where the parameters describe properties on the fixed radius or volume-averaged values, but when analyzing the identity experiments, for instance current alignment, local spatially dependent forms have to be used.

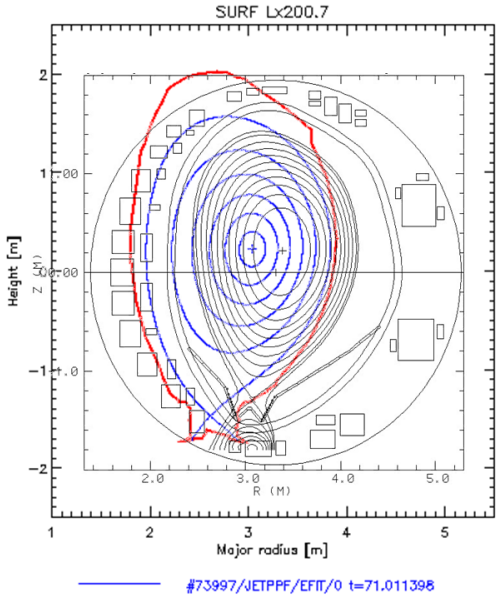

Figure 12: Comparing plasma configuration in identity plasma experiments: JET #74740 (blue and red), JT-60U #49469 (grey).

In pure identity plasma experiments, the dimensionless plasma parameters are set to match without scaling. These experiments require quite same-size devices with similar properties for heating and current-drive systems, in contrast to similarity experiments, where plasma parameters, such as temperature, are set to match within the scope of scaling laws [25]. In these experiments, which are described more specifically in the following subsection, matching of the plasma shape was as convenient as possible between different but same-size devices, which can be seen in Figure 12.

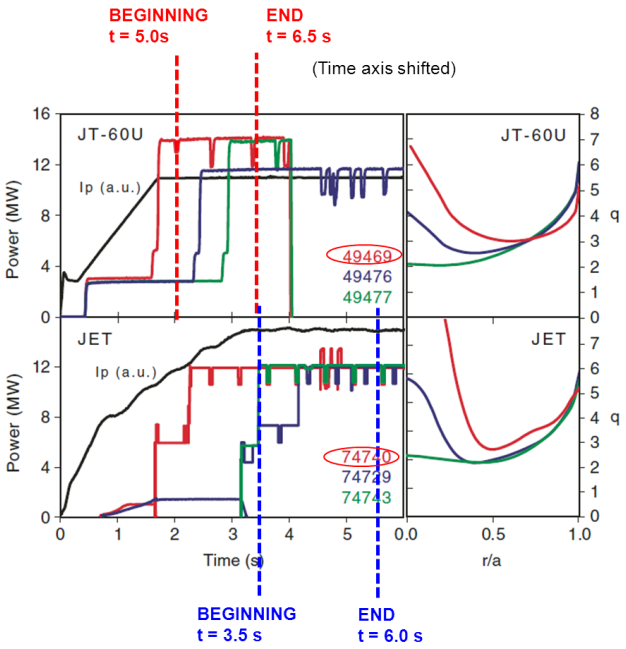

Figure 13: The time interval between the beginning and the end of the analysis.

4.1 Data analysis based on identity plasma experiments in JET and JT-60U

Identity plasma experiments were done in 2008 at JET and JT-60U for studying the different confinement properties and current profile time evolution in advanced tokamak scenarios [6, 7]. From the experiments, one shot from JET (#74740) and one shot for JT-60U (#49469), which are the most comparable for the reverse-q scenario simulations, were selected.

The most common way to describe the identity properties is by comparing the time evolution of the the dimensionless parameters [25], especially the q-profile, in this case. The best correspondence of the q-profile (at the beginning of shots) in JET and JT-60U was detected between shots #74740 and #49469 in the time interval which is presented in Figure 13. Hence, these shots have been selected for more extensive analysis. The matching between the dimensionless plasma parameters and temperature and density profiles are presented

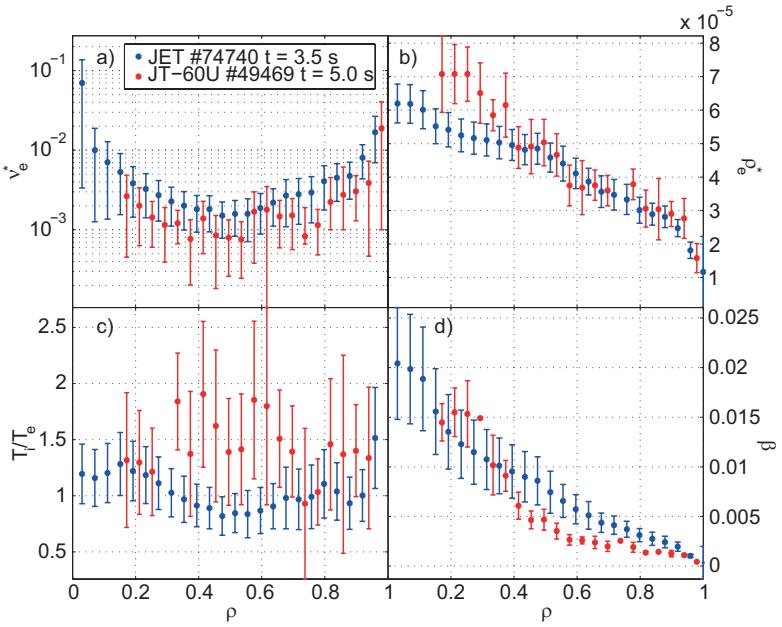

Figure 14: Dimensionless parameters (ν^*, ρ^*, β, T_i/T_e) of shots #74740 (JET) at $t = 3.5$ s (blue) and #49469 (JT-60U) at $t = 5.0$ s (red): a) collisionality, b) normalized Larmor radius, c) beta, d) temperature ratio.

in Figures 14 and 15 for the shots #74740 and #49469 which show the time point of the best correspondence. The durations of the high-power phase of the shots were 3.8 seconds for #74740 and 2.2 seconds for #49469.

Comparing to identity-plasma experimental results is important to find the major reasons for the most important differences in the time evolution of plasma properties that can be described with the dimensionless plasma parameters: safety factor, collisionality, normalized Larmor radius, beta and temperature ratio. The aim of this data analysis and the following simulations is to find the cause for these differences.

Variation of dimensionless plasma parameters of all shots during identity experiments is presented in Table 1. The most significant dissimilarities in parameter values of the selected shots were different inverse aspect ratio ε and plasma current (approximately 30 % larger total current in JET) which causes different ratio of current components, especially the amount of ohmic current, and larger critical bootstrap current (defined by Equation (60)).

4.2 Motivation of the modelling work: Differences between selected shots in JET and JT-60U

Matching of the plasma parameters and configuration at the beginning of the selected reverse-q shots #74740 (JET) and #49469 (JT-60U) has been presented in the previous section in Figures 14 and 15 and the maximum differences in

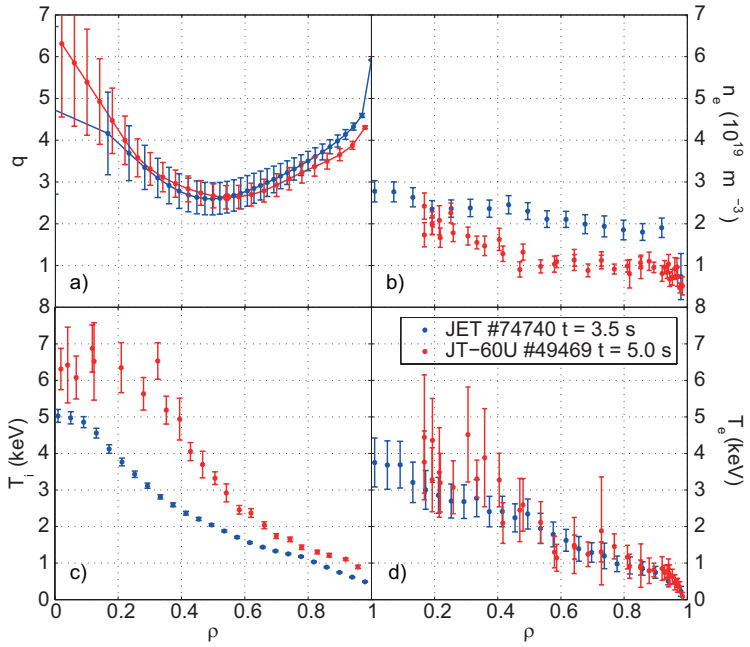

Figure 15: Temperature, density and q profiles of shots #74740 (JET) at $t = 3.5$ s (blue) and #49469 (JT-60U) at $t = 5.0$ s (red).

dimensionless parameters of all identity shots in Table 1. In this section, the main point is to study dissimilarities which can be observed in the plasma parameters a few seconds after starting point (time scale has been marked in time trace plot in Figure 13). These profiles are presented in Figures 16 and 17.

Matching of the plasma parameters, which was achieved in these identity experiments with shots # 74740 and # 49469, was reasonably successful with most of the parameters (presented in Figures 16 and 17). Ion temperature at $t = 3.5$ s in JET and $t = 5.0$ s in JT-60U were the same within 2 keV. The electron temperature and q were similar within errorbars, and ν^*, ρ^* and T_i with acceptable 15% errors (differences outside the half radius were smaller than 10% and in the central plasma 15%). The largest dissimilarities could be observed in the electron density (in Figure 17b). In JT-60U, the minimum of q and a density ITB are localised at the same position at $\rho = 0.5$, whereas in JET a density gradient at the same position could not be observed.

Parameters sustained the matching with the exception of the q-profile (Figure 17a). Also β (Figure 16d) is different, which is caused by the different electron density profile (Figure 17c). Normalised Larmor radius is the same (maximum difference in the central plasma is approximately 15%). Beta and electron density, q and temperature profiles match outside half radius. Maximum differences (inside the half radius) in temperature are 1 keV. Density gradient in JT-60U is larger by a factor of 3 than in JET at beginning, but later

Table 1: Varying of the dimensionless plasma parameters of identity shots in JET and JT-60U [6].

	JET	JT-60U
R (m)	3.1	3.3
a (m)	0.9	0.8
R/a	3.45	4.13
k	1.62	1.60
δ	0.22	0.23
B_0 (T)	2.3	2.3
I_p (MA)	1.5	1.1
q_{95}	4.2	4.2
δ_{TF} (%)	0.008, 0.3, 0.75	0.3
P_{NBI} (MW)	12–14	10–14
$H_{IPB98(y,2)}$	0.95–1.2	1.0–1.2
β_N	1.7–2.2	2.0–2.2
$\beta_{tor,i}$ (%)	0.4–0.55	0.44–0.51
$\rho^* \times 10^{-3}$	4.2–4.5	4.3–5.0
ν_e^*	0.06–0.12	0.09–0.18
$\langle \nu^* \rangle$	0.2–0.3	0.3–0.4
T_i/T_e	1.1–1.4	1.3–1.5
M_Φ	0.06–0.35	-0.2–0.03

it increases even 10 times larger. In JET, a density ITB does not form, and the reverse-q shape is lost totally during 3 seconds.

The most significant difference between the shots of JET and JT-60U are the density gradient and the shape of the q-profile. The density gradient is presented in Figure 18, where it can be noticed that a transport barrier is not observed in the density profile time evolution in JET. Instead, the shot #49469 in JT-60U has a rather strong density gradient at $\rho = 0.15$–0.50, which produces a considerable peak in the bootstrap current density profile. The bootstrap fraction (presented in Figure 19) in JET is less than 30%, whereas in JT-60U the fraction is even 90 % and as high as 40 % also in the later phase. These are significant contributions in the total plasma current when neutral beam fraction and possible other externally induced current components are taken into account.

Neutral beam fractions in the both devices are approximately the same: in JET with the time-averaged NBI current density, the fraction is 22%, and for JT-60U 24%. On the contrary, the main difference between NBI-current properties is the shape of the NBI current density profiles which are illustrated in Figure 20 and whose calculation methods are covered in Section 5.1. The current component given by NBI is larger by a factor of 2 in JET inside the half radius. In JT-60U, the maximum values are located in the half major radius area instead of the central plasma at ρ= 0–0.2 which is the peak position in JET. This kind of flat NBI alignment is possible in JT-60U due to the off-axis beams of NBI system. Commonly it has been thought that a JT-60U-like profile is more favourable for steady-state operation because it advances to sustain a

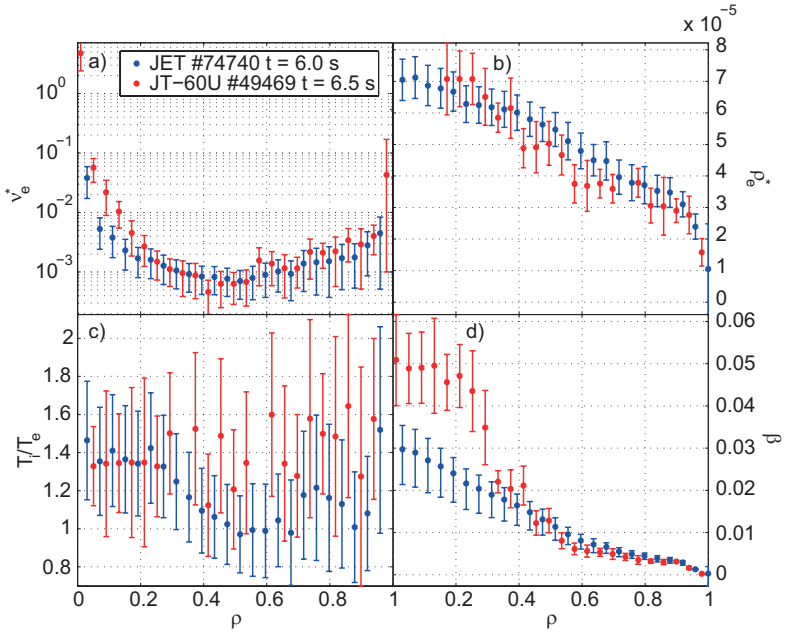

Figure 16: Dimensionless parameters of shots #74740 (JET) at $t = 6.0$ s (blue) and #49469 (JT-60U) at $t = 6.5$ s (red): a) ν^*, b) ρ^*, c) T_i/T_e, d) β.

hollow current profile in the center of plasma. Approximately 50% of the total NBI current is localized inside of $\rho = 0.4$ in JET, but in JT-60U the same fraction was only 30%.

Table 2: Values of current components (MA) at two radial locations.

		I_{NBI}	I_{BS}	I_{OHMIC}
JET #74740	$\rho = 0.4$	0.16	0.105	0.23
	$\rho = 1.0$	0.33	0.32	0.85
JT-60U #49469	$\rho = 0.4$	0.077	0.41	-0.11
	$\rho = 1.0$	0.27	0.80	0.03

However, the impact of the small differences (total NBI current was around 0.3 MA in both devices, so the difference between fractions inside $\rho = 0.4$ was smaller than 0.1 MA) in the NBI current profile is not that significant for the time evolution of the plasma current, in case NBI current is not a dominant part of the total current. Impact of a different NBI current density profile on q-profile evolution has been regarded in Section 6.1 by replacing the NBI profile in the simulation in JET with a profile from JT-60U and vice versa.

In the steady-state operation, ohmic current is replaced by maximizing the self-generated bootstrap components and optimizing the shapes of the external current profile components. In the non-inductive scenario aiming to steady

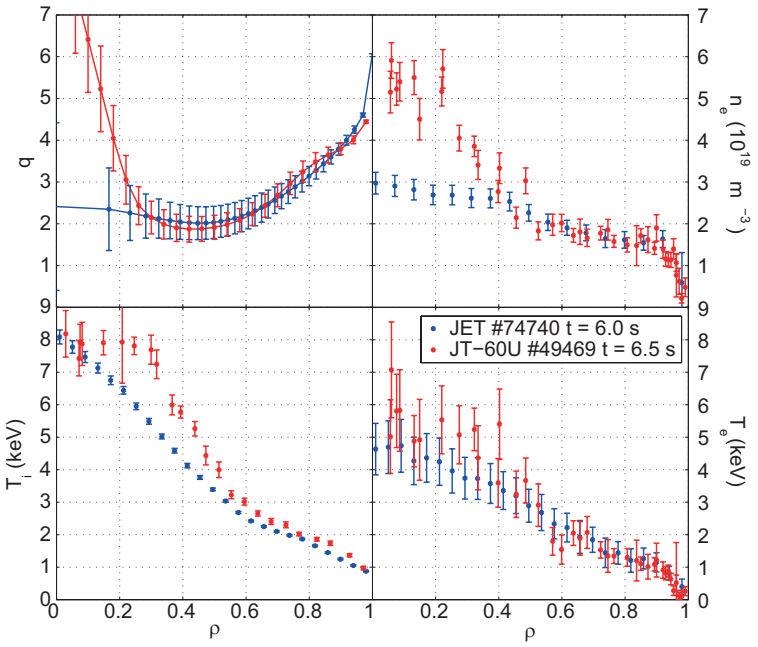

Figure 17: Temperature, density and q-profiles of the shots #74740 (JET) at $t = 6.0$ s (blue) and #49469 (JT-60U) at $t = 6.5$ s (red).

state, the bootstrap fraction should be about 50–70% [6] depending on the externally produced non-ohmic current drive facilities. Figure 19 presents the bootstrap fraction during the identity shots related to this work. JT-60U is much closer of the required fraction of a non-inductive scenario, which can be noticed also by studying the fractions of the ohmic current components at $t = 6.0$ s (JET) or $t = 6.5$ s (JT-60U) in Table 2. The total ohmic current in JT-60U is less than 0.3%, and inductive current is not needed at $\rho < 0.4$ (negative ohmic current). In JET, the ohmic fraction is substantial: 57% at full radius and 47% at $\rho = 0.4$.

The analysis with the critical bootstrap current confirms the observations of the properties, such as electron density and bootstrap fraction, which cause the different time evolution. The negative ohmic current component and the low NBI current inside $\rho = 0.4$ decrease the need for bootstrap current at t = 6.5 s (which is seen in the formula of the critical bootstrap current and Figure 21). According to these results, a steady-state scenario might not be achievable with JET plasma properties of the shot #74740 due to the high critical bootstrap current and the high fraction of inductive current component.

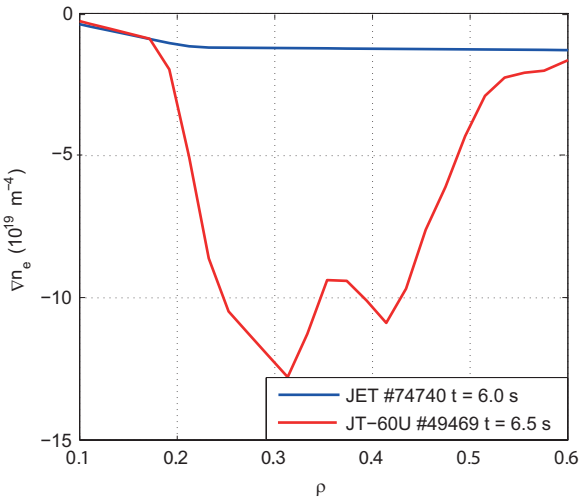

Figure 18: Density gradients in JET and in JT-60U: JET #74740 $t = 6.0$ s (blue), JT-60U #49469 $t = 6.5$ s (red).

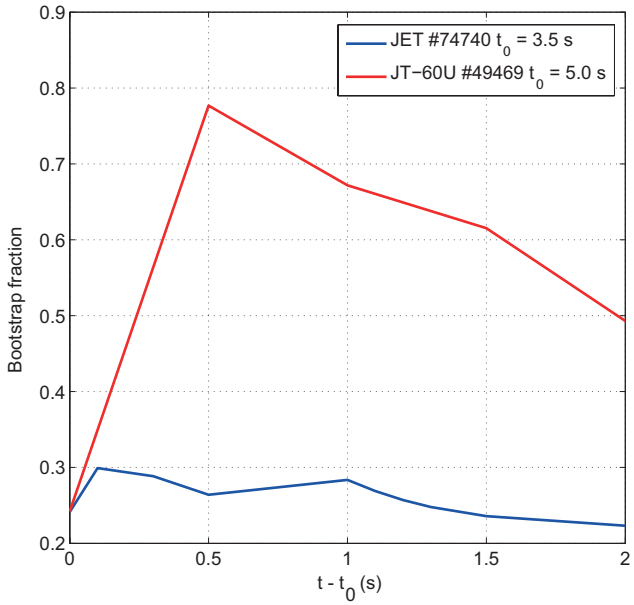

Figure 19: Bootstrap fraction (j_{bs} calculated by NCLASS). Starting point is t_0 which corresponds to 3.5 s in JET #74740 (blue) and 5.0 s in JT-60U #49469 (red).

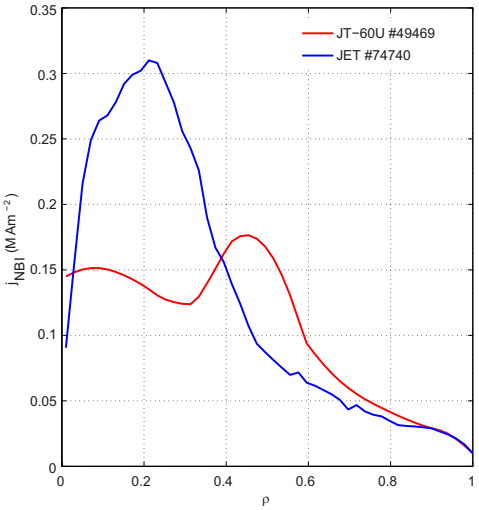

Figure 20: Neutral beam current density calculated by ASCOT in JET #74740 (blue) averaged over the time interval 3.5–6.5 s and in JT-60U #49469 (red) at $t = 6.5$ s.

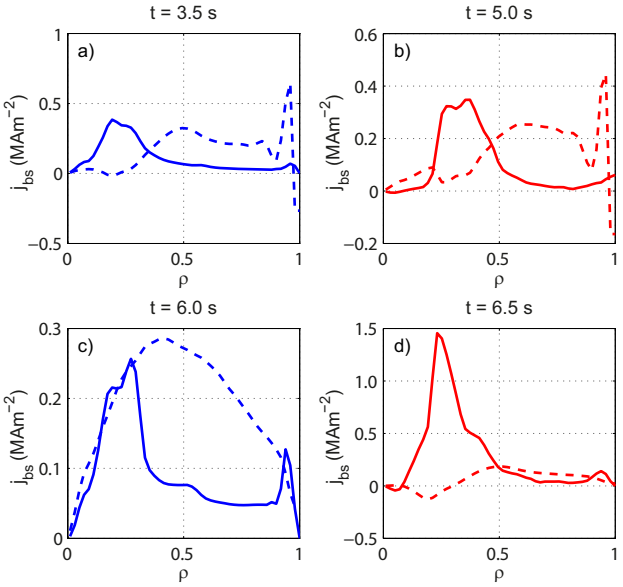

Figure 21: Bootstrap current densities (solid line) and critical bootstrap current densities (dashed line) in the reference simulations in the initial and later phase: JET (blue), JT-60U (red).

5 Current diffusion model and validation

As the input for the simulations, the experimental data which was smoothed and checked with experimental results was used. Plasma parameters in the initial state are presented in Section 4, clarifying the modelling case and validation in Section 5.2 and comparing the NBI-calculation methods in Section 5.1. [6, 7]

Simulations have been performed by using the JETTO [8] code which has been presented in Section 3.2 and whose interaction with other coupled codes and experimental methods is schematically shown in Figure 22. A current profile consists of ohmic current, neutral beam current and self-generated bootstrap current. Neoclassical approach is used in modelling of current density profile with the NCLASS [26] code which calculates the bootstrap current density and (neoclassical) resistivity [8].

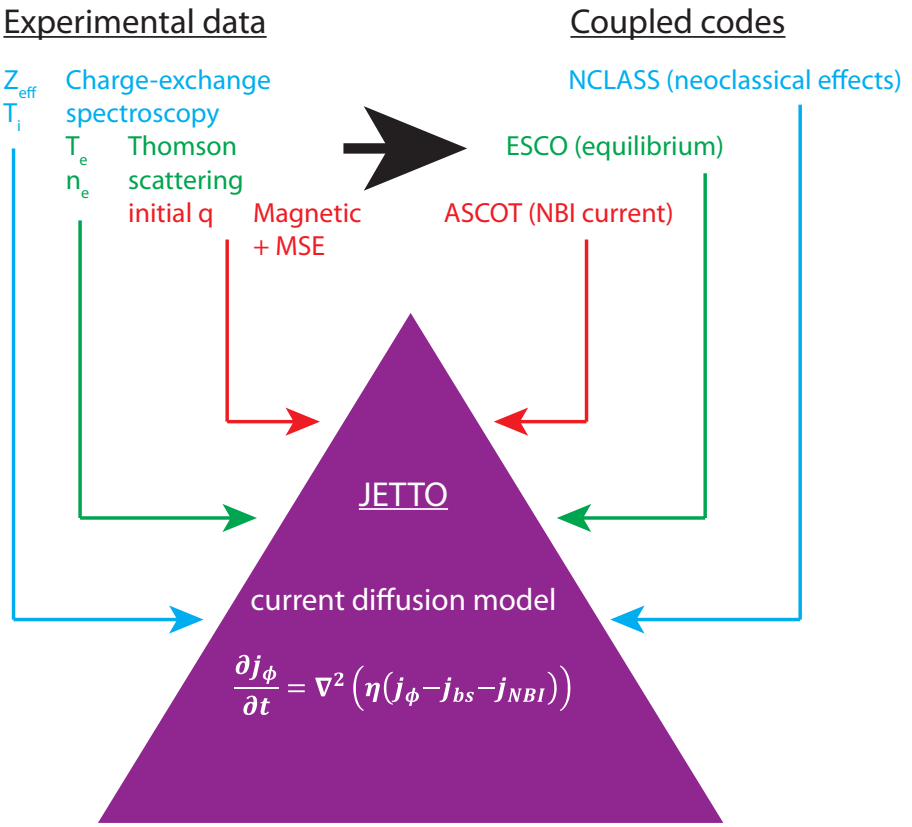

Figure 22: Interaction between JETTO and other coupled codes.

5.1 Testing of different neutral beam computing options

Neutral beam injection current (NBI current) is the most common way to produce external non-inductive plasma current in the recent tokamaks. Since in this case, neutral beam current fraction is over 20% of the total plasma current, computing of it has a significant role in the results of the simulations. Due to

the better consistency with JT-60U (NBI-current density profile from $t = 6.5$ s is available), time-averaged NBI current density profile was selected for use in the current diffusion simulations. For this purpose, testing of the NBI-current computing options has been performed before validation of the JETTO current diffusion model. The goal of these simulations is to compare the effect of time dependence in the neutral beam current profiles, and after that to clarify the differences of current profile components with predictive JETTO simulations.

There are several options of neutral beam codes connected to JETTO. In these testing simulations, NBI current density is calculated with the fast particles orbit-follow code ASCOT [23], which is the most reliable way to determine NBI current. The simulation has been performed using both time-dependent and time-averaged neutral beam current density profiles.

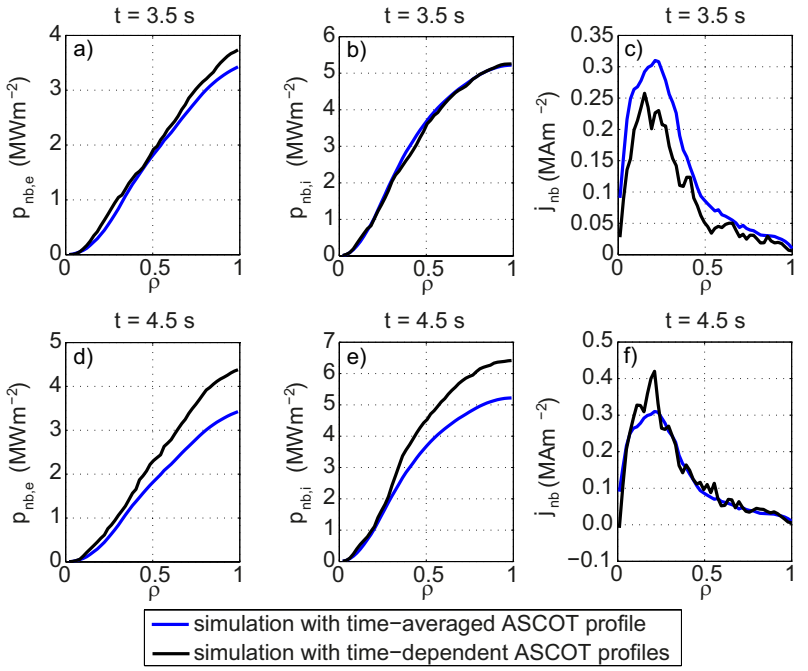

Figure 23: NBI current density profiles and NBI power densities (at $t = 3.5$ s: a) electron power density, b) ion power density, c) NBI current density, at $t = 4.5$ s: d) electron power density, f) ion power density, g) NBI current density) in the testing simulation by the ASCOT code with shot #74740 (JET). Time-dependent (black) and time-averaged (blue) (averaged time interval was 3.5–6.0 s).

Time-dependent data from the discharge #74740 in JET (T_i and Z_{eff} from charge-exchange spectroscopy, T_e and n_e from high-resolution Thomson scattering and q from MSE-EFIT every half second and MSE-EFIT equilibrium at $t = 3.0$ s) was used in the interpretative simulations testing the NBI current. The duration of the NBI validation simulations was 3.5 seconds (from 3.0 s to 6.5 s) to make the simulation time sufficiently long to show the energy transfer

from fast neutral particles to electrons and ions or changes in the current profile in the current diffusion time scale.

Figure 23 shows that the differences in absorbed power and current density profile are small. The maximum difference between time-averaged and time-dependent NBI current density is achieved at $t = 3.5$ s (non-steady-state NBI-current density profiles from earlier time points are not valid or required for using predictive current diffusion simulations) at $\rho = 0.8$, and it causes only a 3% difference in the total current density profile. As a result, the time-averaged NBI current profile can be selected for use as a reliable method in the subsequent predictive current-diffusion simulations.

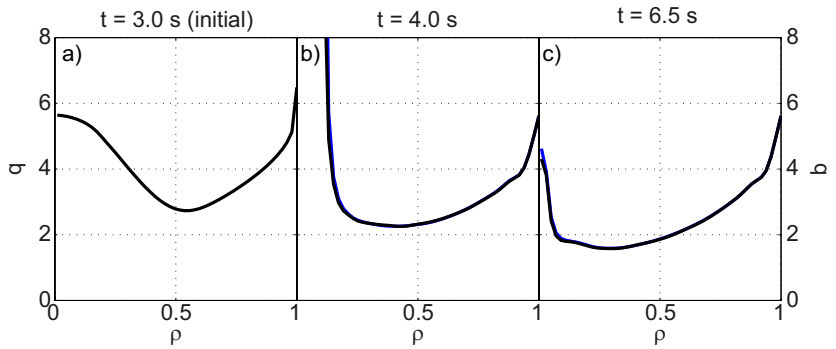

Figure 24: q profile during the predictive JETTO simulation (j_{nbi} calculated by ASCOT) code with shot #74740 (JET). Time-dependent (black) and time-averaged (blue) j_{nbi} (averaged time interval 3.5–6.0 s).

Also the predictive current diffusion simulations with NBI current density profiles from these simulations were implemented by using same input data and ESCO equilibrium to check possible effects on the q-profile. The difference in predicted q-profile time evolution is negligible if time-dependent or time-independent NBI-current density profiles given by ASCOT are used, and this time evolution can be seen in Figure 24.

In these testing simulations an ASCOT version which is connected to the JETTO code has been used. With this version, the ripple losses cannot be taken into account, which can bring a minor inaccuracy for the source term j_{nbi} used in these studies. However, the ripple of the shot #74740 is only 0.30%, so it can be assumed that the ripple effects are not significant in these simulations in the core plasma region. [27]

5.2 Validation of the JETTO model

In the validation of the JETTO current-diffusion model, the same experimental data than in the testing of NBI computing (T_i and Z_{eff} from charge-exchange spectroscopy, T_e and n_e from high-resolution Thomson scattering and q from EFIT-MSE every half second and ESCO equilibrium at t = 3.5 s) in JET discharge #74740 and data profiles from three time points in JT-60U discharge #49469 (T_i and Z_{eff} from charge-exchange spectroscopy, T_e and n_e from high-resolution Thomson scattering and q from magnetic-MSE at t = 5.0 s, 6.5 s and

7.0 s and ESCO equilibrium at t = 5.0 s) were used.

In the validation, the ESCO equilibrium code was used to achieve of the best comparability between JET and JT-60U current-diffusion simulations, since the possible need to calculate the flux functions F requires the same method of determination of the equilibrium. ESCO is the only applicable equilibrium code in JT-60U with JETTO simulations. In JET, ESCO equilibrium results were compared with the EFIT equilibrium corrected with the MSE measurements which is the most reliable experimental safety factor q data. Differences based on this comparison are not significant and ESCO equilibrium was closer to MSE-EFIT than EFIT equilibrium. Testing of the NBI current density has been implemented before the JETTO model validation, and as described in the previous section, ASCOT NBI current density profiles (JET #74740 time-averaged profile from time interval 3.0–6.0 s, JT-60U #49469 profile from t = 6.5 s) were used.

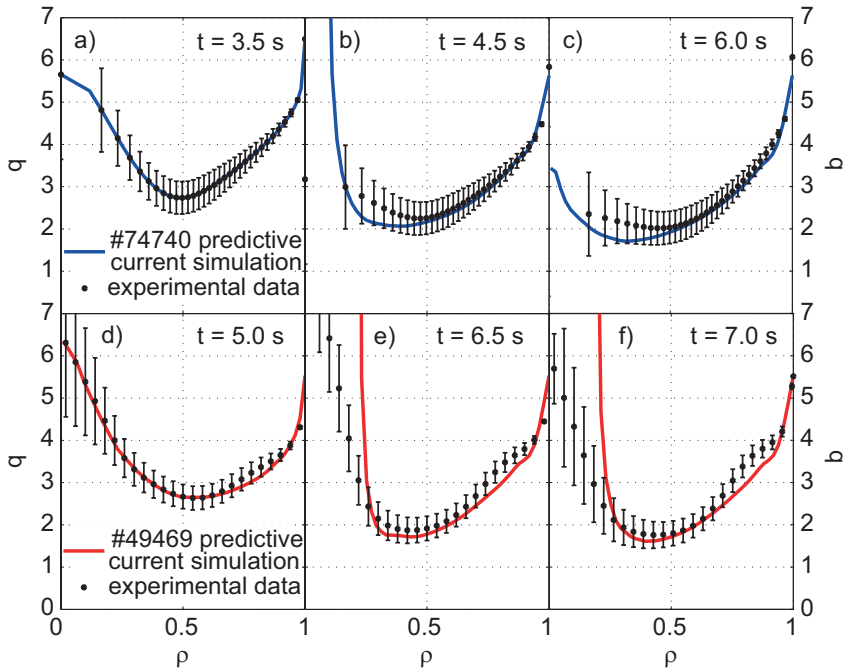

Figure 25: q profile in the validation of the JETTO model (the time interval of simulations JET 3.5–7.0 s, JT-60U 5.0–7.0 s) a) JET #74740 (blue) at t = 3.5 s (initial) b) JET #74740 at t = 6.0 s, c) JT-60U #49469 at t = 5.0 s (initial) d) JT-60U #49469 at t = 6.5 s (red).

The simulated q-profile with experimental values with estimated errors (the weighted statistical errors of 10%, presented for the first time in [6]) are presented in Figure 25. With the time evolution of q in the validation simulations, it can be noticed that the correspondence between the experimental data and the JETTO simulation model is quite reasonable: the largest deviations be-

tween the simulated and experimental values are observed at $t = 6.0$ s in JET and at $t = 6.5$ s in JT-60U in the reverse-q phase. Larger deviations from the estimated errors in the center of plasma can be considered acceptable, since the error bars including systematic errors in the q-profile are difficult to estimate due to the challenging measurement conditions, especially in the center of the plasma.

6 Results of predictive current simulations

The purpose of the predictive current simulations is to clarify the time evolution of the q-profile and its dependence on different current components with two shots: JET #74740 and JT-60U #49469. In the identity plasma experiments, which have been presented in Section 4, the time evolution of many important plasma parameters was studied in two tokamak fusion devices, JET and JT-60U, which are almost of the same size with a similar plasma shape, which is presented in Figure 12 [6].

The steady-state condition with zero poloidal current density and critical bootstrap current has been presented in Section 2.5.2 by Equations (55) and (60). Simulation results have been analyzed also with the approach of the critical bootstrap current. The effects of different electron density profiles and external current density components on the critical bootstrap current and steady-state behaviour have also been studied.

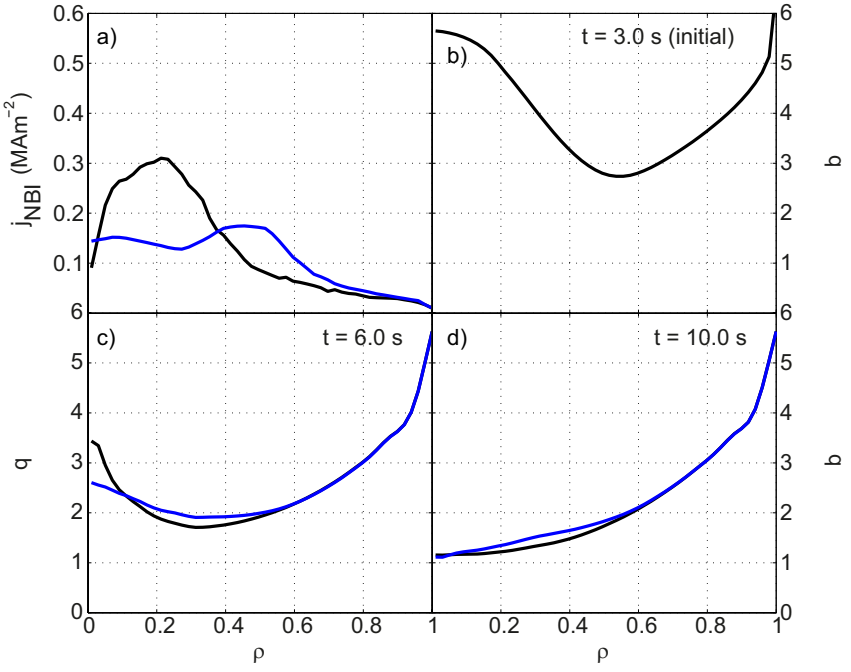

Figure 26: Simulation with replaced neutral beam current density profile in JET: a) used NBI profiles (constant in time) b)-d) q-profile time evolution. Black: reference case in JET, Blue: NBI current density profile from JT-60U.

6.1 Impact of NBI current density profile shape on q-profile

The main objective in two following simulation cases was to understand the reason for the different time evolution of the q-profile which is connected to generating ITBs and fusion efficiency. In these simulations, the same experimental data as in validation was used (described in Section 5.2) with 10-second simulations (time interval in JET #74740 3.0–13.0 s and in JT-60U #49469 5.0–15.0 s). Studying the impact of different NBI-current density profiles has been performed with the simulation cases, where NBI current density in JET was replaced with corresponding profile from JT-60U and vice versa in JT-60U (profiles presented in Figures 26a and 27a).

The behaviour of the q-profile with the replaced NBI-current density and the reference case (equivalent with the simulation of the validation case) has been illustrated in Figures 26 (JET #74740) and 27 (JT-60U #49469). The reference simulations with pure experimental data are presented with black lines and simulations with replaced NBI current density profiles in blue (JET) and red (JT-60U) in the same plots.

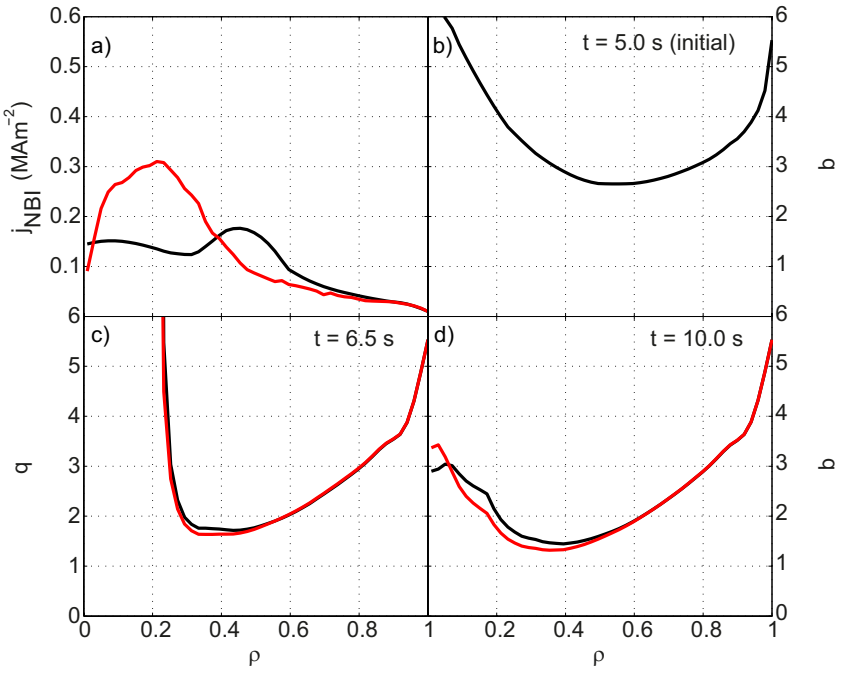

Figure 27: Simulation with replaced neutral beam current density profile in JT-60U: a) used NBI profiles (constant in time)b)-d) q-profile time evolution. Black: reference case in JT-60U, Red: NBI current density profile from JET.

The results in the figures state that the shape of the profile was not a significant property for controlling the current-density time evolution. Maximum

differences with the reference case are 10% (at $\rho = 0.25$–0.40) which are smaller than the estimated errors in the experimentally defined q. As mentioned, the differences between NBI current density profiles were sufficiently large only at $\rho < 0.5$, and the NBI-current fractions were approximately the same. Simulations with larger differences, for instance different NBI-current fractions, could be performed, but this way does not give answers for the different time evolution in these identity experiments with fixed properties.

6.2 Impact of electron density profile

The most significant factor in the bootstrap current is the density gradient. This can be seen in the Equation (35) which gives a rough approximation on the dependence of the pressure gradient components. As mentioned before, the density gradient is the most important difference between the shots of JET and JT-60U. In these sets of simulations which are described in this and the following section, the effects of the density gradient on the bootstrap fraction are studied. Comparing to the shots #74740 and #49469 with the following

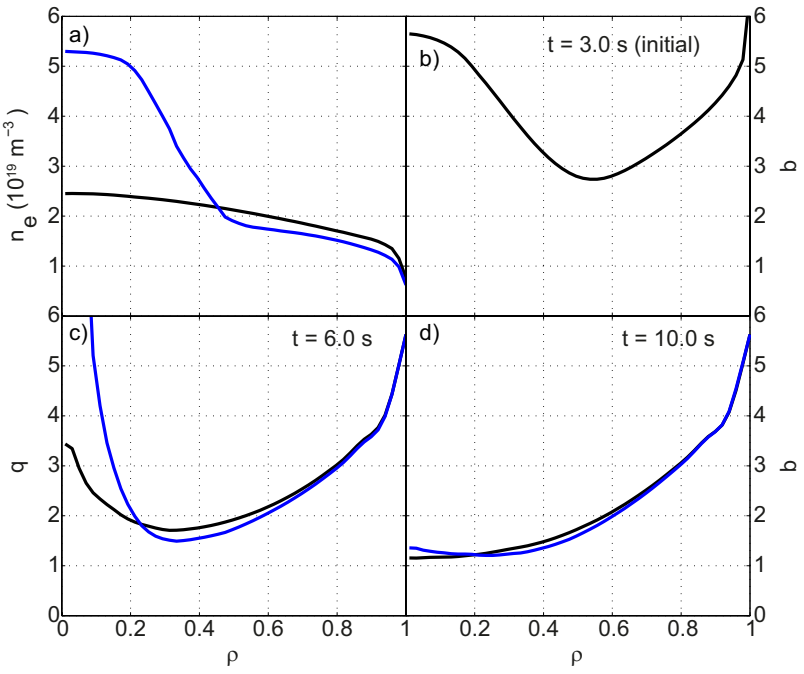

Figure 28: Simulation with replaced electron density profile in JET: a) used electron density profiles (constant in time) b)-d) q-profile time evolution. Black: reference case in JT-60U, Blue: electron density profile from JT-60U.

predictive current simulations (time intervals in JET 3.0–13.0 s and in JT-60U 5.0–15.0 s), the most important role of the electron density profile was established. This can be noted in a simulation case where the electron density

profile in JET was replaced with the profile from JT-60U (#49469 at $t = 7.0$ s with the largest density gradient at $\rho = 0.25$–0.5) and in JT-60U with profile from JET (#74740 at $t = 3.0$ s). The replaced electron density profiles which have been used in the simulations were constant in time and include the cases with the strongest (in JT-60U) and the smallest (in JET) gradients during the identity shots. The reference cases and other data which were used were the same as in the validation case in Section 5.2.

In JET, the electron density profile was replaced with the profile with the strongest gradient from JT-60U at $t = 7.0$ s (presented in Figure 28a). The time evolution of the q-profile has been studied with a 10.0-s simulation whose results have been presented in Figure 28b-d. Then the reverse shape can be seen to be a few seconds longer than in the reference case, but the stationary q-profile is a flat. In the reference case, the reverse shape disappeared at $t = 8.5$ s and with replaced density profile it stayed until $t = 11.0$ s. After 7.0-s simulation differences between the simulated and reference cases are negligible.

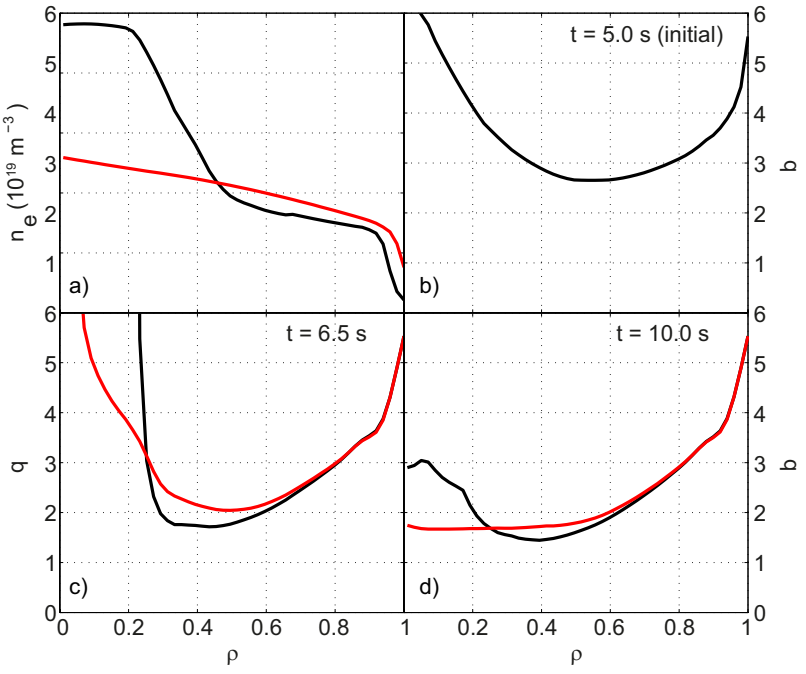

Figure 29: Simulation with replaced electron density profile in JT-60U: a) used electron density profiles (constant in time) b)-d) q-profile time evolution. Black: reference case in JT-60U, Red: electron density profile from JET.

Electron density profile in JET was quite stable, and the profile from time point $t = 6.0$ s was used for replacing the electron density profile in JT-60U at $t = 5.2$ s. In JT-60U simulation, the electron density profile was replaced at the time point $t = 5.2$ s, in which case there is no density ITB during the simulation.

Then q profile gets a flat shape after a 5.0-s simulation. The minimum value of q located at the half-radius area cannot been observed, which can be seen in the results in time evolution in Figure 29b-d.

Interpretation of the steady-state properties is done by studying the critical bootstrap current condition. Bootstrap currents and critical bootstrap currents calculated by Equation (60) have been presented with the experimental cases in Figure 30. Satisfying of the critical bootstrap condition compared with the experimental cases shows that the same density gradient gives a larger effect on the bootstrap current, which can be seen in Table 3. The bootstrap fraction in JET with the replaced density profile is smaller by approximately a factor of two than in JT-60U, which means 0.13 MA less bootstrap current in JET. Since the difference in temperature is minor, electron density is the most significant property in increasing the bootstrap current.

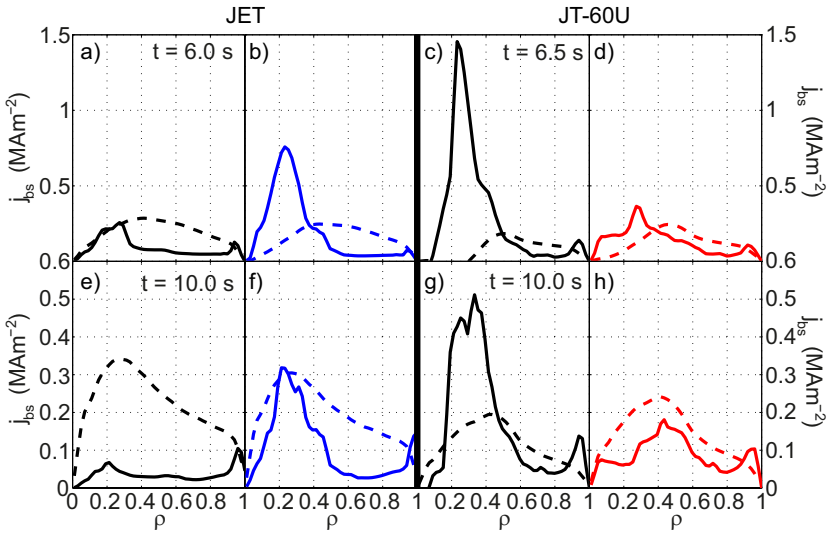

Figure 30: Bootstrap current density (solid line) and critical bootstrap current density (dashed line) in the experimental reference case (black) and in replaced electron density profile simulation: JET #74740 left side, JT-60U #49469 right side.

Table 3: Bootstrap fraction in different replaced electron density simulations.

		JET reference simulation	**JET (n_e replaced)**	**JT-60U reference simulation**	**JT-60U (n_e replaced)**
time point	**6.0 s/6.5 s**	20%	33%	62%	38%
	10.0 s	11%	23%	48%	27%

Another issue, which causes the difference in the bootstrap fraction and the critical bootstrap current, is the inverse aspect ratio ε. The inverse aspect ratio

profiles have been presented in Figure 31, where it can be noticed that the maximum local difference given by ε is 15–18%. The results and the bootstrap fractions in Table 3 show that the critical bootstrap condition is satisfied only in JT-60U with these properties. The bootstrap fraction in JT-60U is larger than in JET with smaller electron density gradient, so it can be assumed that the same gradient produces a larger bootstrap fraction and better bootstrap alignment in JT-60U. Assuming and producing sufficient bootstrap fractions have been discussed in the following section by studying bootstrap fractions with different electron density gradients.

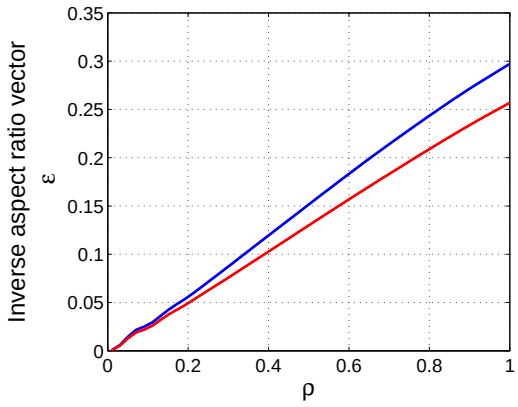

Figure 31: Inverse aspect ratio profile in JET (blue)and in JT-60U (red)

6.3 Effects of electron density gradients for the increasing bootstrap fraction in JET

Impact of the density gradient on the total current density varies between the tokamaks due to different inverse aspect ratio and bootstrap fraction. In JT-60U, the same density gradient is more efficient to increasing the bootstrap current than in JET. In addition, forming the density gradients is more difficult in JET. This makes it challenging to induce good conditions for steady-state operation, so in such case a larger fraction of the total current has to be produced with the external current-drive methods. In JT-60U, the bootstrap fraction is 50% or larger at every time point, being thus at least 1.5 times larger than in JET. This fraction does not appear to be achievable in all tokamaks, which can be seen in the following results by testing different electron-density profiles and stronger gradients.

The case of 10-second simulations which have been implemented with four different density gradient for the shot #74740 in JET and comparing them with each other and the reference case (same than in validation case in Section 5.2) are described. The same experimental data as in the validation case was used in these simulations with the exception of the replaced density profiles (four different density profiles and gradients are presented in Figure 32a). The experimental electron-density profiles were replaced at $t = 3.5$ s with different density

gradient cases. Otherwise, the same experimental data was used as the input for these simulations as in the reference case which has been described before.

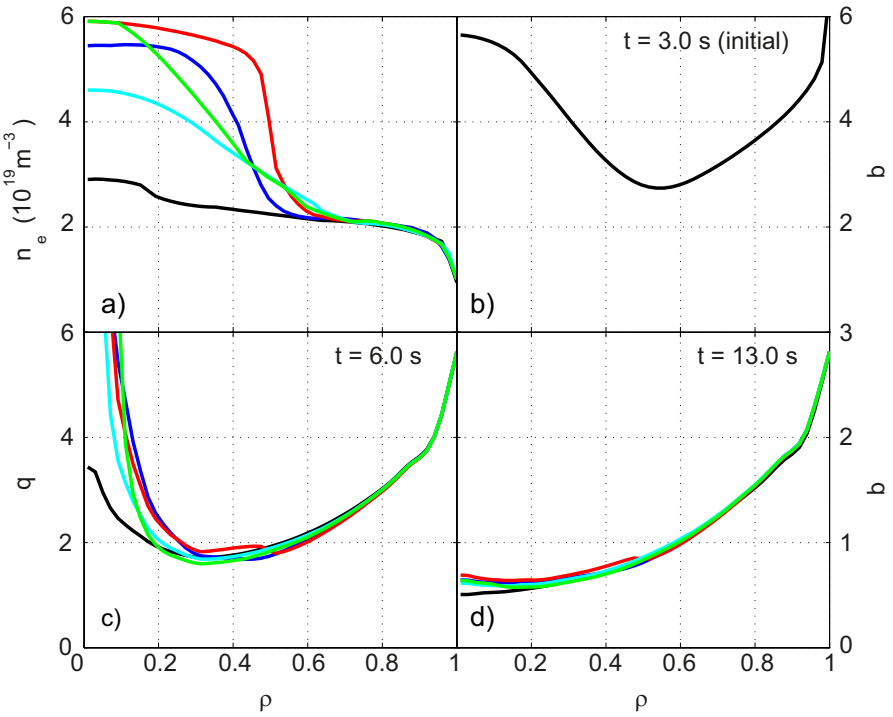

Figure 32: Simulation with different electron density profiles (cases same as in Table 4): a) electron-density profiles (constant profiles in time), b-d) q-profile time evolution.

The equivalent predictive current-density simulations are shown in Figure 32b-d in which it can be seen that even very steep density gradients (the gradient in the red case is more than 10 times larger than in reference at $t = 3.5$ s) cannot maintain the reverse shape of the q-profile in JET for 10 seconds. Experimentally, the reverse shape of q is maintained for 3.0 seconds, and in the case of the steepest gradient (red) the reverse shape can be observed still after 5 seconds, but the shape becomes flat before 10 seconds. In JT-60U, a lower density gradient can give rise to a larger bootstrap fraction and the reverse shape of the q-profile remained at least until 2.0 s, which can be seen in the experimental results (in the simulations, the reverse shape is observed still after 15 seconds). The bootstrap fractions in JET with different density gradients have been presented in Table 4. The values indicate that the fractions are smaller than in JT-60U in every case, so with these observations it can be noticed that no density gradient can sustain the reverse shape of the q-profile. The bootstrap-current density remains below the critical bootstrap condition in every case, since the produced bootstrap current is localized inside $\rho = 0.5$

which is the same position with the density gradient, as shown in Figure 33.

Table 4: Bootstrap fraction in different density-gradient simulations.

		case 1 (blue)	**case 2 (red)**	**case 3 (green)**	**case 4 (cyan)**	**JET reference (black)**
time point	**6.0 s**	38%	43%	38%	32%	20%
	10.0 s	28%	38%	28%	25%	11%

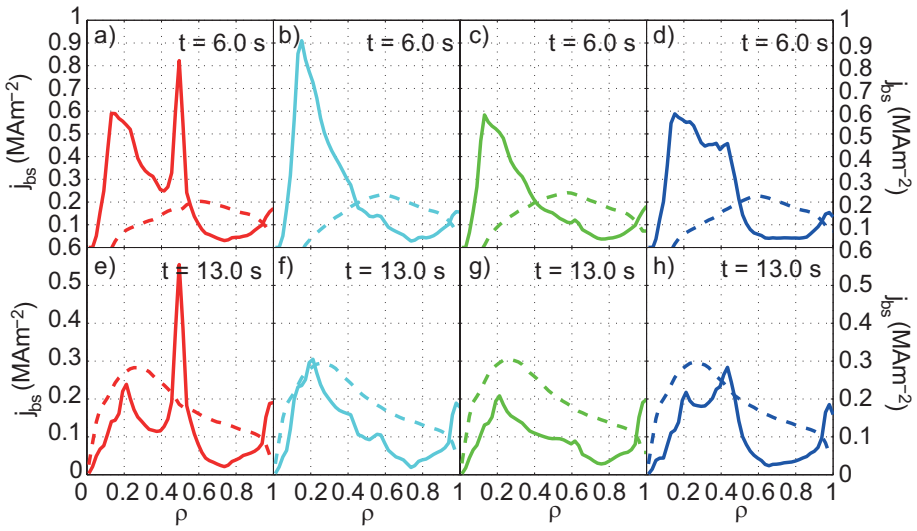

Figure 33: Bootstrap current densities and critical bootstrap current densities in JET with different density gradients: a–b) case 1, c–d) case 2, e–f) case 3, g–h) case 4.

The reasons for the role of the different inverse aspect ratio in the bootstrap current which can be seen in Equation (60) or the reasons for the time evolution of the density are challenging to clarify, since the simulations with different ε can not be performed. The relevance of the critical bootstrap current and current alignment has been discussed, which can give more information on the connection between the current profile and the steady-state conditions. Another considerable issue is generating the required density profiles and gradients. The diffusion and transport processes in the plasma are very nonlinear, so the simulations with predictive temperature and density profiles have to be used to understand the causality between electron density and the current-density profile and the differences in JET and JT-60U.

6.4 Impact of the added externally produced non-ohmic current components

As previously mentioned, generating the strong and stable density gradient on the half radius in JET is very challenging, so the residue of the ohmic plasma current is replaced with the non-inductive external methods. Due to nonlinearity, the impact of different (externally or internally generated) current components should be unequal, in which case, by increasing the fraction of the external current components, a beneficial result is not achieved. For instance, the bootstrap fraction is connected to temperature- or density transport phenomena and different plasma profiles (gradients), which cause different confinement.

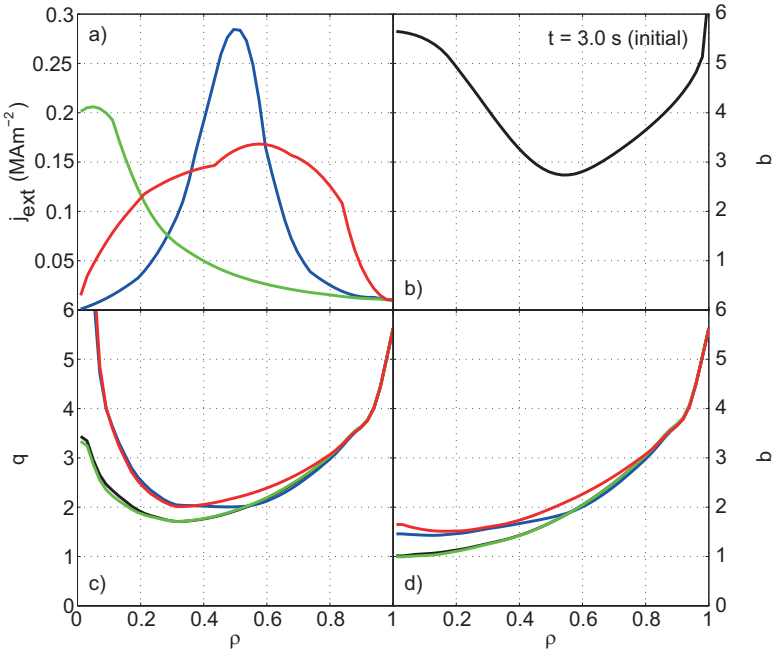

Figure 34: Simulation with different externally produced current components (cases same as in table 3): a) added current density, b-d) q-profile time evolution.

Table 5: Bootstrap fraction in different simulation cases of added external current-density profiles.

		case 1 green	**case 2 blue**	**case 3 red**	**JET reference (black)**
time	**6.0 s/6.5 s**	20%	33%	62%	38%
point	**10.0 s**	11%	23%	48%	27%

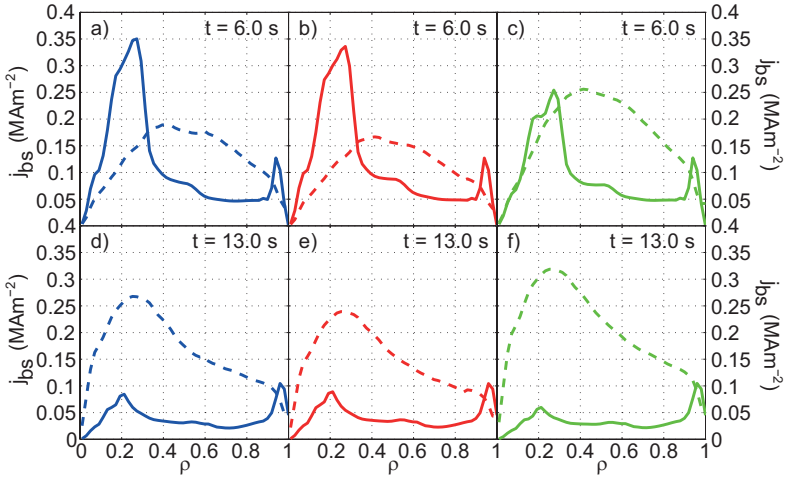

Figure 35: Bootstrap current and critical bootstrap currents in simulation with different externally produced current components (the colour codes same as in Figure 34).

By this set of simulations, the effects of a few different added current density profiles on the q-profile time evolution in JET have been studied. The experimental data of the shot #74740 is used as the input for these several current-diffusion simulations with a reference case without any added current components. The most significant observations of three different externally produced current densities which correspond to different current fractions (case 1 23%, case 2 31%, case 3 9%) are presented in Figure 34. During the 10.0-second simulation the reverse q-profile has not remained, as can be seen Figure 34d. In case 1, the reverse shape disappears after 5 seconds and the behaviour of the q-profile is approximately identical to the reference. In cases 2 and 3, it is sustained for 7 seconds. With the larger current fraction in cases 1 and 2 the reverse shape can be sustained for a few seconds longer than in the reference case but here the current fractions above 20 % are required, and after 10 seconds the q-profile is a flat also in these cases.

The critical bootstrap current condition in Equation (60) gives the same results in Figure 35: fulfilling the condition is not possible in JET with this kind of scenarios. The critical bootstrap current density is 2–3 times larger than the obtained bootstrap current density which is not sufficiently large. The need for non-ohmic current is the largest at $\rho > 0.5$ but the non-ohmic components (j_{nbi} and mostly added j_{ext}) of these simulations are localized closer to the centre of the plasma.

7 Summary and conclusions

In this thesis, the theoretical background of neoclassical phenomena related to current diffusion has been clarified on the required level. The results of identity plasma experiments between two same-sized tokamaks JET and JT-60U, have been analysed and compared. Current-diffusion modelling with the 1.5-dimensional transport code JETTO has been performed based on the experimental data. Differences in the time evolution of the current components and the q-profile have been studied and the approach of the critical bootstrap current has been applied to drawing conclusions on the steady-state properties.

The parameters in the identity shots #74740 (JET) and #49469 (JT-60U) have been successfully matched in the initial state, but after a few seconds the time evolution of q and electron density n_e take a different trend. Notwithstanding the good matching of the dimensionless parameters and temperature profiles, the fractions for the ohmic current are different. In JT-60U the need for the ohmic current is considerably smaller, but in JET the ohmic current is the most significant component of the total plasma current.

The effects of the non-inductive current components have been studied by simulations where the NBI-current density profile or the electron density were replaced with different profiles. These results say that sustaining the reverse-shaped q is very difficult in JET; even an almost six times larger density gradient is not able to sustain it for longer than 5 seconds. In JT-60U, the reverse shape (q_{min} is localized at $0.3 < \rho < 0.4$) is kept for over a 15-second simulation with the experimental electron density profile, so it can be assumed that the reverse q is steady state.

The steady-state conditions with the critical bootstrap current density have been compared between the selected discharges. The need for the critical bootstrap current depends on the ohmic current density, which can be seen in the derivative of Equation (60) where a time-independent j_{nbi} has been assumed. This equation shows that even small variations (small time variations which can be observed for example in the temperature profile or gradient) in the bootstrap-current density cause non-stationary behaviour of the need for bootstrap current. Hence, a completely stationary state can be achieved only by satisfying the condition of stationarity defined by the critical bootstrap-current density. This can be seen in the connection between the ohmic and the bootstrap-current time evolution in Figures 36 and 37 where the varying in the residual current density profile and the ohmic current density are illustrated. The need for the critical bootstrap current decreases during first few seconds, whereas in JET it increases.

The critical bootstrap current condition which is equal to zero poloidal current density and negative F' was satisfied in JT-60U in these simulated cases. Equation (56) shows that the negative F' increases the effect of a pressure gradient on the total current density, which can also be seen in the results. The same pressure gradient produces a larger bootstrap-current density in JT-60U than in JET where the positive F' reduces the net effect of the total pressure gradient for the current density.

The effect of the different inverse aspect ratio has been analysed in Section 6.2. The effect is noticeable but not the most significant. In JET, the non-ohmic current fraction was lower in principle due to higher total current (in JET $I_p = 1.5$ MA, in JT-60U $I_p = 1.1$ MA) which is required in the matching

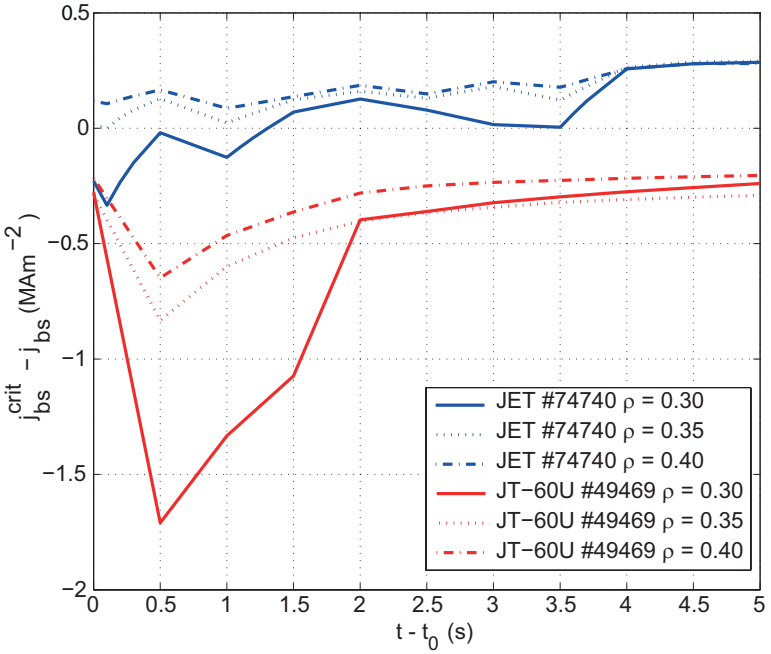

Figure 36: Time evolution of the difference between the critical bootstrap current and bootstrap current (NCLASS) in the ITB region ($0.3 < \rho < 0.4$). Starting point is t_0 which corresponds to 3.5 s in JET #74740 (blue) and 5.0 s in JT-60U #49469 (red).

of the plasma parameters.

The ohmic current in three time points has been presented in Figure 37, where it can be seen that the need for critical bootstrap current decreases in the time interval 5.0–6.5 s in JT-60U. In JET, increasing the bootstrap or non-ohmic current fraction by decreasing the total plasma current ($I_p = 0.9$ MA) helps to sustain the reverse q longer (10 seconds or more), but here the minimum value of the q is located closer to the central plasma (from $\rho = 0.55$ to $\rho < 0.30$). As earlier mentioned, small variations in temperature and density profile have an important role in achieving the steady state and fulfilled the critical current density condition. By using the time-independent data profiles for temperature and density, stationary state with fulfilled critical current density was achieved in smaller total current (and larger bootstrap fraction).

Probably, the most significant error source in the analysis of the critical bootstrap current density is the rough approximation of the bootstrap current in Equation (57). This form does not take into account the different contributions from electron and ion temperature or density gradients. The sign of the bootstrap current driven by ion temperature gradient is negative but the approximative form gives positive current and it cannot see different gains in the terms of the total pressure gradient either. The form with the correction term can give more reliable results if only a computing method with better accuracy

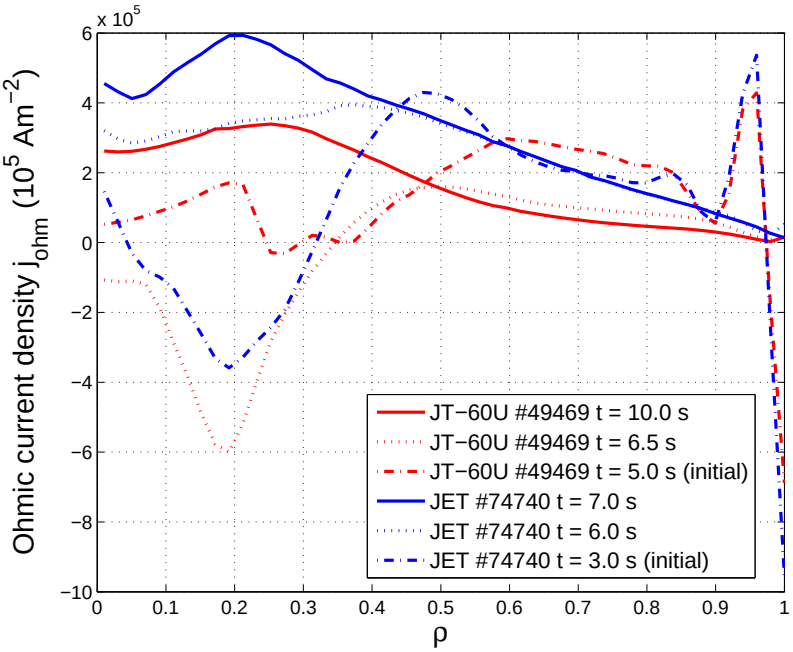

Figure 37: Ohmic current density in JET (blue) #74740 $t = 3.0$ s (dash-dot), $t = 6.0$ s (dot), $t = 7.0$ s (solid) and JT-60U (red) #49469 $t = 5.0$ s (dash-dot), $t = 6.5$ s (dot), $t = 10.0$ s (solid).

is used to define the bootstrap current density profile. In this analysis, NCLASS code was used and its error sources were not clarified in these cases. Extended and more reliable analysis with the critical current density condition requires studying the cases by codes with better accuracy and different approach; kinetic neoclassical computing, for example. The differences between the approximative and corrected form of the critical current density condition varied from 1–2% to over 100% but further studies are required to draw any quantitative conclusions based on the scale of errors.

The reasons which cause forming of the steep density gradient in JT-60U are not clearly clarified in the previous analysis [6]. The large density ITB has not been observed experimentally in JET with this kind of conditions, and on the basis of these simulations, steep density gradients in the beneficial region $0.25 < \rho < 0.6$ would not help to sustain the reverse shape of q for longer than 5–10 seconds and also, adding of external current does not lead to fulfilling of the steady-state condition.

The cause for the electron density peaking which was one of the most significant differences between discharges #74740 and #49469 was not clarified by this analysis. For this, predictive temperature and density simulations are required and will be the focus of further studies in future.

References

[1] Ongena J. et al. 2000. Energy for future centuries — prospects for fusion power as a future energy source, Transactions of Fusion Technology **37** 3–15.

[2] Lawson J.D. 1957. Some Criteria for a Power Producing Thermonuclear Reactor. Proceedings of the Physical Society B **70** 6.

[3] ITER Physics Basis (updated). Overview and Summary. 2007. Nuclear Fusion **47** S1–S17.

[4] Rebut B.H. et al. 1985. The Joint European Torus: installation, first results and prospects. Nuclear Fusion **25** 1011.

[5] Taylor T.S. et al. 1997. Physics of advanced tokamaks. Plasma Physics and Controlled Fusion **39** B47.

[6] Litaudon X. et al. 2011. Core Transport Properties in JT-60U and JET Identity Plasmas. Nuclear Fusion **51** 073020.

[7] de Vries P. C. et al. 2009. Identity physics experiment on internal transport barriers in JT-60U and JET. Plasma Physics and Controlled Fusion **51** 124050.

[8] Cenacchi G., Taroni A. 1988. JETTO: A Free-boundary Plasma Transport Code (Basic Version). Rapporto ENEA RT/TIB/88/5.

[9] Cordey J.G. et al. 1988. The bootstrap current theory and experimental evidence. Plasma Physics and Controlled Fusion **30** 11 1625–1635.

[10] Kikuchi M. 1990. Steady state tokamak based on the bootstrap current. Nuclear Fusion **30** 265.

[11] Wesson J. 2004. Tokamaks. 3rd edition. Oxford University Press.

[12] Zohm H., de Blank H. J. (editors). 1995. Summer University for Plasma Physics 25–29.9.1995, Max-Planck-Insitut fur Plasmaphysik (Course material).

[13] Peeters A.G. Introduction to neoclassical transport. 2000. (Course material)

[14] Peeters A.G. 2000. The bootstrap current and it consequences. Plasma Physics and Controlled Fusion **42** B231.

[15] Kessel C.E. 1994. Bootstrap current in a tokamak. Nuclear Fusion **34** 1221.

[16] Litaudon X. 2006. Internal Transport Barriers: critical physics issues? Plasma Physics and Controlled Fusion **48** A1–A34.

[17] Garcia J. Giruzzi G. 2012. Conditions for the sustainment of high-beta stationary scenarios in tokamaks. Plasma Physics and Controlled Fusion **54** 015009.

[18] Wagner F. et al. 1982. Regime of improved confinement and high beta in neutral-beam-heated divertor discharges of the ASDEX tokamak. Physical Review Letters **49** 1408–1412.

[19] Lao L. et al. 1985. Reconstruction of current profile parameters and plasma shapes in tokamaks. Nuclear Fusion **25** 1611.

[20] Koch R. 1998. Plasma heating: NBI & RF. Transactions of fusion technology **33** 2T.

[21] Fisch N.J. 1987. Theory of Current Drive in Plasmas. Reviews of Modern Physics. **59**.

[22] Challis C.D. et al. 1989. Nuclear Fusion **29** 563.

[23] Heikkinen J.A. et al. 2001. Particle Simulation of the Neoclassical Plasmas. Journal of Computational Physics **173** 527–548.

[24] Ongena J. et al. 1998. Numerical transport codes. Transactions of Fusion Technology **33** 2T.

[25] Luce T.C. et al. 2008. Application of dimensionless parameter scaling techniques to the design and interpretation of magnetic fusion experiments. Plasma Physics and Controlled Fusion **50** 043001.

[26] Houlberg W.A. et al. 1997. Bootstrap current and neoclassical transport in tokamaks of arbitrary collisionality and aspect ratio. Physics of Plasmas **4** 9.

[27] Salmi A. et al. 2008. ASCOT Modelling of Ripple Effects on Toroidal Torque. Contributions to Plasma Physics **48** 77–81.